MicroRNA-155 negatively affects blood-brain barrier function during neuroinflammation.

Journal Item

MicroRNA-155 negatively affects blood-brain barrier function during neuroinflammation

Short title: Brain endothelial miR-155 in neuroinflammation

Miguel Alejandro Lopez-Ramirez[1,6], Dongsheng Wu[1], Gareth Pryce[2], Julie E. Simpson[3], Arie Reijerkerk[4,7], Josh King-Robson[2], Oliver Kay[2], Helga E. de Vries[4], Mark C. Hirst[1], Basil Sharrack[5], David Baker[2], David Kingsley Male[1], Gregory J. Michael[2], Ignacio Andres Romero[1]

[1]Department of Life, Health and Chemical Sciences, Biomedical Research Network, The Open University, Milton Keynes, UK., [2] Center for Neuroscience and Trauma, Blizard Institute Barts and The London School of Medicine and Dentistry, London, Queen Mary University of London, UK., [3]Sheffield Institute for Translational Neuroscience, University of Sheffield, Sheffield, UK., [4]Blood-Brain Barrier Research Group, Molecular Cell Biology and Immunology, VU University Medical Center, Amsterdam, the Netherlands., [5]Department of Neurology, Sheffield Teaching Hospitals NHS Trust, University of Sheffield, Sheffield, UK.

Correspondence: Ignacio A. Romero, Department of Life, Health and Chemical Sciences, Biomedical Research Network, The Open University, Walton Hall, Milton Keynes, MK76AA, United Kingdom. Tel. +44 1908 659467; Fax. +44 1908 654167; email: i.romero@open.ac.uk

[6]Current address; Yale Cardiovascular Research Center, Section of Cardiovascular Medicine, Yale University School of Medicine. New Haven, CT 06511, USA., [7]to-BBB, J.H. Oortweg, 2333 CH, Leiden, the Netherlands.

Abbreviations:

BBB, blood-brain barrier; MS, multiple sclerosis; miRNAs, microRNAs; CNS, central nervous system; EAE, experimental autoimmune encephalomyelitis; IJC, interendothelial junctional complex; MS-NAWM, MS normal appearing white matter; LPS, lipopolysaccharide; BEC, brain endothelial cell; ECM, extracellular matrix; OS, onset of signs; APP, acute phase paralysis; LCM, laser capture microdissection; hCMEC/D3, human cerebral microvascular endothelial cell line; PFA, paraformaldehyde; ISH, *in situ* hybridization; DOCK-1, dedicator of cytokinesis 1; SDCBP, syntenin-1; PALLD, palladin; ITGAV, integrin alpha-V; ANXA-2, annexin-2; CLDN-1, claudin-1; PRNP, prion protein; SSC, saline sodium citrate; PBS, phosphate buffer saline; 3'UTR, 3'untranslated region; RT, room temperature; SEM, standard error of the mean.

Abstract

Blood-brain barrier (BBB) dysfunction is a hallmark of neurological conditions such as multiple sclerosis (MS) and stroke. However, the molecular mechanisms underlying neurovascular dysfunction during BBB breakdown remain elusive. MicroRNAs (miRNAs) have recently emerged as key regulators of pathogenic responses although their role in central nervous system (CNS) microvascular disorders is largely unknown. Here, we have identified miR-155 as a critical miRNA in neuroinflammation at the BBB. MiR-155 is expressed at the neurovascular unit of individuals with MS and of mice with experimental autoimmune encephalomyelitis (EAE). In mice, loss of miR-155 reduced CNS extravasation of systemic tracers both in EAE and in an acute systemic inflammation model induced by lipopolysaccharide. In cultured human brain endothelium, miR-155 was strongly and rapidly upregulated by inflammatory cytokines. MiR-155 upregulation mimicked cytokine-induced alterations in junctional organization and permeability whereas inhibition of endogenous miR-155 partially prevented cytokine-induced increase in permeability. Furthermore, miR-155 modulated brain endothelial barrier function by targeting not only cell-cell complex molecules such as annexin-2 and claudin-1 but also focal adhesion components such as DOCK-1 and syntenin-1. We propose brain endothelial miR-155 as a negative regulator of blood-brain barrier function that may constitute a novel therapeutic target for central nervous system neuroinflammatory disorders.

Key Words:

Multiple sclerosis, neurovascular dysfunction, junctional complex molecules, focal adhesion.

Introduction

In neuroinflammation, stroke and some neurodegenerative diseases such as multiple sclerosis (MS), the permeability of the blood-brain barrier (BBB) increases, contributing to the onset and/or worsening of the disease. Although the mechanisms are not completely understood, it is thought to involve disassembly of interendothelial junctional complex (IJC) and integrin focal adhesion complexes (1-3), probably as a result of altered expression of tight junctional proteins in response to pro-inflammatory cytokines such as TNFα and IFNγ (4-6). *In vitro* these cytokines increase brain endothelial cell (BEC) permeability by modulation of gene expression at transcriptional and/or post-transcriptional levels (3, 5, 7) . Recently, microRNAs (miRNAs) have emerged as important additional post-transcriptional regulators of gene expression which can silence target genes by translation inhibition, mRNA decay or both (8). Indeed, miRNAs might constitute an important regulatory control of the brain endothelial response by fine-tuning several of the cellular and molecular processes triggered by inflammatory mediators (7). Furthermore, deregulated miRNA levels have been demonstrated in several pathologies although their role in the pathogenesis of central nervous system (CNS) inflammatory disorders remains to be fully elucidated.

One of the best-characterized miRNAs is miR-155, which has pleotropic functions in inflammation, autoimmunity and cell plasticity (9-11). Thus far, miR-155 has been shown to induce a decrease in the expression levels of multiple identified transcripts but the effect is modest, characteristic of fine-tuning regulation (12, 13). Moreover, endothelial miR-155 has been shown to regulate the expression of endothelial nitric oxide synthase during inflammatory stimuli (14). In the context of neuroinflammation, miR-155 has been shown to be one of the most highly elevated miRNAs in acute MS lesions (15). At a functional level, loss of miR-155 partially protects mice from the development of experimental allergic

encephalomyelitis (EAE), a model of MS (10, 16). This correlates with its actions in promoting differentiation of TH17 cells (17), inhibiting TH2-type immune responses and mediating activation of T cells, mononuclear phagocytes and dendritic cells (10, 18, 19). However, since the symptoms of EAE are related to increased BBB permeability, it is equally possible that miR-155 is acting directly in BECs to modulate BBB function.

In this study, we demonstrated altered levels of miR-155 at the neurovascular unit in MS brains and EAE spinal cords. MiR-155$^{-/-}$ mice showed lower levels of BBB leakage in EAE and an acute model of systemic inflammation. Mechanistically, we found that miR-155 regulated human brain endothelial permeability by targeting molecules involved in cell-to-cell, annexin-2 and claudin-1, and cell-to-extracellular matrix (ECM) interactions, DOCK-1 and syntenin-1. Our results demonstrate that brain endothelial miR-155 negatively regulates BBB function thereby constituting a novel therapeutic target for MS and other neuroinflammatory conditions associated with BBB breakdown.

Materials and methods

*Human and animal tissues***.** Human brain samples of MS patients and control patients without neurological diseases were obtained from the UK Multiple Sclerosis Tissue Bank (Imperial College London, London, UK). Adult male and female (10–12 weeks) Biozzi ABH mice were purchased from Harlan UK Ltd (Bicester, UK) whereas miR-155$^{-/-}$ mice and miR-155$^{+/+}$ C57BL/6 mice were from Jackson Laboratory (Kent, UK). All procedures were approved following ethical review processes in accordance with the Animals (Scientific Procedures) Act 1986 of the UK government and the ARRIVE guidelines (20).

*Induction of experimental autoimmune encephalomyelitis***.** EAE was induced in Biozzi ABH mice with 1mg freeze-dried mouse spinal cord homogenate in Freund's adjuvant supplemented with 60mg *Mycobacterium tuberculosis* H37Ra and *Mycobacterium butyricum* as previously described (20). In miR-155$^{-/-}$ or miR-155$^{+/+}$ C57BL/6 (B6.Cg-miR-155tm1.1Rsky/J) mice, EAE was induced using Hooke Kit™ (EK-2110) MOG35-55/CFA Emulsion PTX following the manufacturer's protocols (Hooke Laboratories, Lawrence, MA, USA). Animals were monitored daily to assess the development of relapsing–remitting paralysis and scored as follows: 0=normal; 1=limp tail; 2=impaired righting reflex; 3=hind-limb paresis and 4=complete hind-limb paralysis (20). The EAE status were based on paralytic clinical disease and weight loss/gain as follows: Onset of signs (OS), clinical score 1 with weight loss sampled on day 15 post-induction; Acute phase paralysis (APP), clinical score 3.5-4 and losing weight on day 17; Recovery, clinical score 3.5 to 1 with weight gain on day 20; Remission one, clinical score 0.5 with weight gain on day 28 post-induction; Chronic, clinical score 3.5 with stable weight during remission from attack 3 months following induction (20).

Laser capture microdissection and isolation of microvessels. Laser capture microdissection (LCM) was used to collect enriched brain endothelium RNA using a rapid staining protocol described in the Supplementary Methods online (21).

Microvessels were isolated from the mouse spinal cords as previously described with modification (22). Briefly, EAE or normal ABH mice were perfused with Hank's balanced solution containing 0.5% BSA to rinse out the blood, then the spinal cords were flushed out. The spinal cords were digested with collagenase and dispase (1mg/ml) at 37^{o}C for 1h, then homogenized and centrifuged through 25% BSA, the pallet of microvessels was undergone a second digestion for 30min and purified via passing through a 70μm size mesh filter.

RNA extraction and microarray analysis. Immortalized human cerebral microvascular endothelial cell line (hCMEC/D3) was cultured as described previously (3). Total RNA from three biological replicates were isolated using miRNeasy mini kit (Qiagen, Sussex, UK) according to the manufacturer's protocols. Whole EAE and control spinal cords or isolated spinal microvessels were homogenized using TRIzol reagent according to the manufacturer's protocols. Total RNA of vessels via LCM was extracted with RNAqueous-micro kit following the manufacturer's protocol (Ambion, Life Technologies Ltd, Paisley, UK). The quantity (NanoDrop 1000 spectrophotometer) and the quality (2100 Bioanalyzer, RNA 6000 Pico LabChip; Agilent, Palo Alto, CA, USA) of the total RNA were analysed. Detailed procedures and complete microarray data are available at the Gene Expression Omnibus (GEO) under accession number GSE44694 (www.ncbi.nlm.nih.gov/geo).

Quantitative RT-PCR. TaqMan® MicroRNA Reverse Transcription Kit (Applied Biosystems, Warrington, UK) was used to synthesise single-stranded cDNA according to the manufacturer's protocol. Briefly, 2.5 ng of total RNA in the case of LCM material and 10 ng

of total RNA in the case of spinal cords, isolated spinal microvessels or cultured cells were used to synthesis single-stranded cDNA. Specific RT and PCR primers for hsa-miR-155 (000479-4427975), mmu-miR-155 (002571-4427975), hsa-miR-24 (000402-4427975) or RNU6B (001093-4440887), internal control, were obtained from Applied Biosystems (Warrington, UK). TaqMan® Universal PCR Master Mix (Applied Biosystems, Warrington, UK) was used to determine the relative levels of hsa-miRs, mmu-miR1-55 and RNU6B. The reaction was then placed in a thermal cycler (DNA engine Opticon 2, Bio-Rad, CA, USA) using an initial step at 95 °C for 10 min for activation, followed by 40 cycles (15 s at 95 °C, 60 s at 60 °C) according to the manufacturer's protocol. The method $2^{-\Delta\Delta CT}$ was used for analysis of the data (23). Each control value for each experiment (unstimulated cells, whole spinal cords of control mice, microvessels from control human brains or mouse spinal cords) was normalized to one and treatment or disease values are always represented as relative to control values. SYBR Green real-time PCR (Qiagen, Manchester, UK) was used to determine the relative levels of murine *claudin-5,* (forward) CCTTCCTGGACCACAACATC and (reverse) CGCCAGCACAGATTCATACA; *pecam-1,* (forward) GGACGATGCGATGGTGTATAA and (reverse) GCATCACTGTGCATTTGTACTT; *gfap,* (forward) CAGAGGAGTGGTATCGGTCTAA and (reverse) GATAGTCGTTAGCTTCGTGCTT; *cd45,* (forward) CCCTTCTTCTGCCTCAAAGT and (reverse) CACCTGGATGATATGTGGTCTC, whereas *actin,* (forward) CTCCCTGGAGAAGAGCTATGA, (reverse) CCAAGAAGGAAGGCTGGAAA, mRNA levels were used as an internal control. The method $2^{-\Delta CT}$ was used for analysis of the data (23), results were expressed as relative abundance.

Immunohistochemistry and in situ hybridization. EAE mice in acute phase grade 4 (n = 5) and control mice (n = 5) were perfused with 4% paraformaldehyde (PFA) in 0.1M phosphate

buffer. After cryoprotection in sucrose and freezing, 15 µm sections of lumbar spinal cords were cut onto SuperFrost Plus slides (VWR, Leicestershire, UK). Sections were first treated with 2 µg/ml proteinase K in 100mM Tris HCl pH 7.5 and 50 mM EDTA at 37 °C for 10 min, then fixed again for 5 min in 4% PFA and dehydrated for 5 min in 70% ethanol. Sections were prehybridised in hybridisation buffer consisting of 50% formamide, 5x saline sodium citrate (SSC), pH 7.0 [20xSSC = 3 M NaCl, 0.3 M tri-sodium citrate] (24), 100 µg/ml sheared salmon sperm DNA and 0.1% Tween-20 at the miR probe hybridisation temperature (52 °C) for 30 min before replacing this with the hybridisation solution containing probe. Double-digoxigenin labelled miRCURY LNA™ probe miR-155 oligonucleotide (5 nM; Exiqon, Vedbaek, Denmark) was hybridised with the sections overnight at 52 °C. A similarly labelled LNA scrambled oligonucleotide (5 nM) with no complementary sequence in the mouse was used as a negative control at the same condition. After hybridisation, sections were washed through a series of 5 min SSC washes maintained at 55°C. Sections were washed three times with 5xSSC, three times with 1xSSC, and three times in 0.2xSSC. Sections were subsequently incubated for 15 min in a blocking buffer consisting of 0.5% blocking reagent (Roche, West Sussex, UK) in TBST (100 mM Tris HCl pH 7.5, 150 mM NaCl, 0.1% Tween-20) prior to incubation overnight in rat anti-PECAM-1 (1:50, BD Biosciences, Oxford, UK) and sheep anti-digoxigenin antibody conjugated with alkaline phosphatase (1:1000, Roche West Sussex, UK). Next, sections were washed with TBST four times, 5 min each, prior to washing in alkaline development buffer (100 mM Tris HCl pH 9.5, 100 mM NaCl, 50mM MgCl2, 0.1% Tween-20), and then incubated in NBT/BCIP (1%, Roche West Sussex, UK), levamisole (0.5%, Vector Labs, Peterborough, UK) in alkaline development buffer at 30°C. After washing with TBST four times, 10 min each, the sections were incubated for 1h with secondary goat anti-rat IgG conjugated to Alexa 488 (1:375, Zymed Invitrogen, Paisley, UK). Next, sections were washed with TBST four times, 5 min

each, before washed in KTBST (50 mM Tris HCl pH 7.5, 150 mM NaCl, 20 mM KCl, 0.5% Tween-20) to reduce the background signal in the in situ. Cell nuclei were stained using Dapi Fluoromount-G obtained from DouthernBiotech (Alabama, USA). Slides were viewed with fluorescent microscope and photographed in colour using a Nikon Eclipse 80i fluorescence microscope, a MBF CX9000 digital camera, and PictureFrame software.

Immunocytochemistry. hCMEC/D3 cells were grown to confluence on collagen-coated Lab-Tek™ multi-well chamber slides. Immunocytochemistry was performed as described previously (3). Briefly, hCMEC/D3 cells were fixed for 10 min at room temperature with 4 % PFA in PBS pH 7.4. To determine the expression of junctional complex molecules and focal adhesions, cells were permeabilized with 0.5% Triton X-100 in PBS for 5 min. Slides were blocked with 0.5% BSA for 30 min and incubated with anti-ZO-1 (1:80, Zymed, Paisley, UK) and anti-vinculin (1:200, Sigma-Aldrich, Dorset, UK). For talin immunostaining, cells were fixed in methanol for 30 min at 4°C followed by cold acetone (maintained at -20°C prior to use) for 1min at RT and incubated with anti-talin (1:300, Sigma-Aldrich, Dorset, UK) antibody. Cells were washed with PBS and incubated for 1 h at room temperature with a secondary goat anti-rabbit or anti-mouse Alexa Fluor 488 (Zymed, Life Technologies Invitrogen division, Paisley, U.K.). Slides were viewed with a fluorescent microscope for talin and vinculin (Olympus BX61,Olympus, Hertfordshire, UK) or a confocal microscope (Leica Microsystems, Mannheim, Germany) for ZO-1 and images captured using Cell^P or Leica application suite (LAS) software, respectively. For confocal microscopy, images of fifteen Z stacks between 2.5µm in depth were acquired using a 100x oil immersion objective and projected onto one image.

Ectopic expression of miR-155 and siRNA transfections. hCMEC/D3 cells were seeded and grown to 70 % confluence in EGM-2 MV medium before transfection then media was changed to EGM-2 MV medium (Lonza, Slough Wokingham, UK) supplemented with the following components obtained from the manufacturer: 0.1% (v/v) rhFGF, 0.1% (v/v) ascorbic acid, 0.04% (v/v) hydrocortisone and 1.25% (v/v) FBS (hereafter referred to as transfection media). To ectopically express miR-155 in hCMEC/D3 cells, 30 nM of pre-miR-155 and the siPORT Amine transfection agent (Applied Biosystems, Warrington, UK) were combined following the manufacturer's instructions. Inhibition of endogenous miR-155 expression was performed by transfection with 60 nM of hsa-miR-155 miRIDIAN Hairpin Inhibitor (Inhibitor-miR-155). To silence human annexin-2 (ANXA-2), dedicator of cytokinesis 1 (DOCK-1), syntenin-1 (SDCBP), and claudin-1 (CLND-1) specific siGENOME SMARTpool were used (ThermoFisher scientific, Epsom, UK). In both cases, inhibitor-miRs and siRNAs were combined with Lipofectamine 2000 (Invitrogen, Paisley, UK) according to the manufacturer's instructions. For all oligonucleotide, siPORT (pre-miRs) or lipofectamine 2000 (Inhibitor-miRs or siRNAs) were diluted in Opti-MEM I medium (Invitrogen, Paisley, UK) according to the manufacturer's protocols. The RNA oligonucleotide-lipofection agent complexes were then dispensed onto the hCMEC/D3 cells and incubated at 37 ºC for 6h (Lipofectamine 2000) or 24h (siPORT Amine). Transfection media with oligonucleotide complexes was then replaced with fresh transfection media for another 20h (Lipofectamine 2000) or 2h (siPORT Amine). hCMEC/D3 cells were then maintained in EGM-2 MV culture media without VEGF until the end of the experiment. Non-Targeting scrambled pre-miR, inhibitor-miR or siRNA pool was used as transfection control respectively.

Lentiviral transduction of 3' UTR reporter vectors and luciferase assay. The luciferase reporter lentiviral vector constructs containing the puromycin resistance gene and the Luciferase gene from the firefly *Photinus pyralis* with the 3'untranslated region (3'UTR) of DOCK-1 (Accession number NM_001380), syntenin-1 (Accession number NM_005625), annexin-2 (Accession number NM_005625) and claudin-1 (Accession number NM_021101) were obtained from Applied Biological Materials Inc. (British Columbia, Canada).

To generate stable hCMEC/D3 cells a multiplicity of infection of three was used for each of the 3'UTR lentiviral constructs. Briefly, hCMEC/D3 cells were seeded to 40% confluence on twenty-four well plates. Cells were transduced with transduction media with the following components: 1 x 10^6 transducing units/ml of the lentiviral vector and 8μg/ml of polybrene, all suspended in EGM-2 medium. After 12h of transduction, the transduction media was removed and fresh EGM-2 medium was added. hCMEC/D3 cells were grown to confluence and then split into six well plates. Next, EGM-2 media containing 2μg/ml of puromycin were used to select transduced cells.

Detection of luciferase was performed using Steady-Glo® Luciferase assay system according to the manufacturer's protocol (Promega, Madison, WI, USA). Cells were grown on collagen-coated white 96 well cell culture microplates (Greiner bio-one). Luciferase activity was detected using a BMG plate reader (Ortenberg, Germany).

Western blot analysis. Cells were lysed by scraping into a lysis solution containing 400μl of RIPA buffer (25mM Tris•HCl pH 7.6, 150mM NaCl, 1% NP- 40, 1% sodium deoxycholate, 0.1% SDS) and a cocktail of inhibitors (5μg/ml of aprotinin, leupeptin, pepstatin and 1mM sodium orthovanadate). After sonication, the amount of protein was determined using a Biorad DC protein assay (Hertfordshire, UK). Cell lysates were diluted in 1x Laemmli's buffer solution, at 95°C for 10 min. 25μg of total protein was run per lane on 12 and 10%

SDS-PAGE gels and transferred onto nitrocellulose membrane (Amersham, Buckinghamshire, UK) using wet transfer system (Bio-Rad, Hemel Hempstead, UK). Membranes were blocked with 5% non-fat milk/0.05% Tween-20 in PBS for 1h, and incubated in the presence of anti-DOCK-1 (1:200, Cell Signaling, Hertfordshire, UK), anti-syntenin-1 (1:100, AbD Serotec, Oxford, UK), anti annexin-2 (1:3000, BD Biosciences, Oxford, UK) and anti-claudin-1 (1:125, Zymed, Paisley, UK) at RT overnight in a humidified box and then with a species-specific secondary anti-rabbit IgG (1:3000, Zymed) or anti-mouse IgG (1:14000, Pierce Biotechnology, Cheshire, UK) antibody conjugated to horseradish peroxidase for 1 h at RT. Immunoblots were then developed by enhanced chemiluminescence detection (ECL, Amersham, Buckinghamshire, UK). As a control for protein loading and transfer, membranes were stripped for 40 min at 50 °C and incubated with monoclonal antibody against actin (1:200, Sigma-Aldrich, Dorset, UK) and revealed as previously.

In vitro paracellular permeability assays. Cells were seeded onto collagen- and fibronectin-coated permeable polyester transwell filter inserts (Corning Costar, Buckingham, UK, 0.4μm diameter pore, 12mm diameter). hCMEC/D3 cells were grown to 85% confluence and transfected as indicated earlier and stimulated for 24h with TNFα and IFNγ (1ng/ml, R&D systems, Oxon, UK) or left untreated. Culture media was then removed from the apical chamber and 500μl of transport buffer (2% FBS in DMEM without phenol red) containing 2mg/ml 70kDa or 4kDa was added. The paracellular flux of tracer was performed as described previously (3).

In vivo BBB permeability assays. On day 21 after induction of EAE, BBB permeability was determined as described previously with modifications (25). Briefly, 70kDa FITC-dextran

(250mg/kg) was injected intravenously, 30 min later mice were transcardially perfused with 0.9% saline (400ml/kg) first and then with 4% PFA (800ml/kg). Lumbar enlargement (L4-5) segments were cross-sectioned at 20μm thickness and mounted with DAPI-fluoromount G. To determine extravascular intensity of FITC-dextran, images were taken using fluorescent microscopy at 40x magnification (Zeiss, Cambridge, UK). Images were quantified with ImageJ software and normalized to fluorescence values in liver and to tissue area.

For the acute model of systemic inflammation, 12 week-old male miR-155$^{-/-}$ or miR-155$^{+/+}$ C57BL/6 mice were injected 2% Evans blue in PBS intraperitoneally at 80 mg/kg. At 18 h, lipopolysaccharides (LPS) from *Escherichia coli* 0111:B4 (4mg/kg, n=6) or PBS alone (n=4) were injected intraperitoneally (26). After 6h, blood samples were collected by cardiac puncture, mice were perfused with ice cold 0.9% saline and whole spinal cords were flushed. Each spinal cord was homogenized in PBS, then mixed with 60% trichloroacetic acid and incubated on ice for 30 min, supernatants were collected by centrifugation at 1000g for 30 min. Absorbances of supernatants and plasma were read at λ 620 nm. Each absorbance value was then normalized to fresh weight of spinal cords and to plasma concentration of Evans blue.

Statistical analysis. Data are represented as mean ± standard error of the mean (SEM). For all experiments, the number of independent experiments, n, is indicated. For miRNA array analysis, GeneSpring GX 9 software was used for value extraction. Statistical significance was determined by Student's t test for each miRNA probe. The statistical analysis for the mRNA microarray was performed using pairwise comparisons and false discovery rate. Statistical significance was considered if *P* was less than 0.01 as determined by LIMMA software. For all other experiments, statistical significance was considered if *P* was less than 0.05 as determined by paired, 2-tailed Student's t test (cultured cells), or by ANOVA

(analysis of variance) with posthoc comparisons and Tukey HSD correction on SPSS software (animals and human brains).

Results

MiR-155 is upregulated at the neurovascular unit of MS active lesions

Our initial investigations started by investigating whether the proinflammatory miR-155 (9) was altered at the level of the neurovascular unit in MS active lesions. In order to isolate the microvasculature of white matter, we used the laser capture microdissection (LCM) technique. We compared miR-155 levels in MS lesions with active, ongoing demyelination and inflammation with MS normal appearing white matter (MS-NAWM) and with those in white matter of non-neurological disease controls. Clinical information and the neuropathological characterization of MS and control tissues used in this study are shown in Figure 1*A*. We observed that MiR-155 at the neurovascular unit in MS lesions was significantly increased when compared to MS-NAWM (Fig. 1*B*) and control-NAWM (data not shown). These results suggest that increased levels of miR-155 at the neurovascular unit could potentially be implicated in BBB dysfunction in MS.

MiR-155 is differentially regulated during EAE and modulates paracellular permeability *in vivo*

To examine the temporal expression pattern of miR-155 *in vivo*, we initially induced EAE in Biozzi ABH mice, an animal model of MS, which show a predictable relapsing-remitting paralysis course associated with loss of BBB integrity at the spinal cord (20). We observed that the expression levels of miR-155 in whole spinal cords did not change at onset of signs (EAE-OS, animals with a tail paralysis) (Fig. 2*A*). However, we observed that miR-155 levels were dramatically elevated in acute phase paralysis (APP) animals with hindlimb paralysis

and during the recovery phase, reaching levels almost 15 times higher than in control animals (Fig. 2*A*). In addition, miR-155 increased levels were observed in the remission from the initial attack and chronic phases following remission from relapses albeit to a lesser extent (Fig. 2*A*). To investigate whether miR-155 was upregulated in the CNS vasculature during EAE, we extracted total RNA from isolated spinal cord microvessels. Fig. 2*B* shows that expression of miR-155 in enriched spinal cord microvessels of EAE mice was 25 times higher than that of enriched microvessels in control mice using quantitative RT-PCR. However, isolated spinal cord microvessels that contain high levels of markers for endothelial cells (*claudin-5* and *cd-31*) also show minor amounts of astrocyte (*gfap*) and leucocyte (*cd-45*) markers (Fig. 2*C*). In order to distinguish the endothelial miR-155 from other CNS resident cells or leucocytes, we carried out *in situ* hybridization in combination with immunohistochemistry for endothelial (PECAM-1) marker in spinal cord of EAE APP mice (Fig. 2*D*, 2*E*). We observed that miR-155 is upregulated in inflamed blood vessel and partially co-localizes with endothelial PECAM-1 and Glut-1 expression (Fig. 2*F*, 2*G*, 2*H,* Supplementary Fig. 1) but not in their control littermates (Supplementary Fig. 1).

These results lead us to investigate whether the resistance of miR-155$^{-/-}$ mice to develop EAE (Fig. 3*A*) (10, 16) was in part associated with a decrease in vascular leakage at the region of inflammation. First, we observed that miR-155$^{+/+}$ and miR-155$^{-/-}$ mice showed a similar levels of leakage to 70kDa FITC-dextran indicating that BBB integrity is maintained in miR-155$^{-/-}$ mice (Fig. 3*B*, 3*C*). Following induction of EAE, the soluble marker was found to be diffused through the spinal cord parenchyma and highly located near to the basolateral domain of inflamed blood vessels indicative of BBB breakdown in miR-155$^{+/+}$ mice (Fig. 3*B*, 3*C*). In contrast to miR-155$^{+/+}$ EAE mice, miR-155$^{-/-}$ EAE mice showed a 50% reduction in the BBB leakage to the paracellular tracer (Fig. 3*B*, 3*C*). However, the reduced BBB leakage observed

in miR-155$^{-/-}$ EAE mice may not only be due to a reduction in immune cell activation (9, 27) but also in part associated to a decrease in neurovascular dysfunction during neuroinflammation.

In order to investigate the role of miR-155 in inflammation-induced neurovascular dysfunction with reduced leucocyte infiltration and/or leucocyte-triggered immune responses such as TNFα secretion (Figure 3*D*), we determined BBB permeability to Evans blue in an acute inflammation model induced by intraperitoneal injection of lipopolysaccharide (LPS). LPS administration induced a 2-fold increase of Evans blue leakage into spinal cords of miR-155$^{+/+}$ mice compared to PBS-treated miR-155$^{+/+}$ mice (Fig. 3*E*). By contrast, no increase in Evans blue extravasation was observed in miR-155$^{-/-}$ mice spinal cords following LPS treatment when compared with PBS-treated miR-155$^{+/+}$ or miR-155$^{-/-}$ mice (Fig. 3*E*). Overall, these results suggest a potential role of miR-155 at the neurovascular unit in the negative modulation of BBB during neuroinflammation.

MiR-155 modulates paracellular permeability of brain endothelium *in vitro*

We have shown evidence of increased levels of miR-155 at the neurovascular unit during neuroinflammation (Fig. 1*B*, 2*B*, 2*F*, 2*G*, 2*H,* Supplementary Fig.1). However, our *in vivo* experiments do not unequivocally exclude indirect effects on neurovascular dysfunction by miR-155 expression in other CNS resident cells including astrocytes and pericytes. To better understand whether endothelial miR-155 directly mediated barrier dysfunction during neuroinflammation, we next investigated whether proinflammatory cytokines altered levels of miR-155 in cultured human brain endothelial cells. Indeed, miR-155 was upregulated in hCMEC/D3 cell-line by two cytokine treatments including TNFα+IFNγ and TNFα+IL1β but not by IFNγ+IL1β (Fig. 4*A*). Furthermore, we observed a time- and dose-dependent increase in miR-155 expression levels in response to TNFα+IFNγ (Fig. 4*B*). We next investigated

whether upregulation of miR-155 was associated with increases in paracellular permeability of BEC. hCMEC/D3 cells were transfected with pre-miR-155 (Fig. 4*C*) and paracellular permeability was assayed. First, we observed that low concentrations (1ng/ml) of TNFα and IFNγ induced 1.9-fold increase in leakage of fluorescent dextrans across brain endothelial monolayers when compared with controls (Fig. 4*D*). Furthermore, the ectopic expression of miR-155 in hCMEC/D3 cells (Fig. 4*C*) induced a 1.5-fold increase in the leakage of both 4kDa (data not shown) and 70kDa fluorescent dextrans (Fig. 4*D*) when compared with scrambled pre-miR transfected cells. In contrast, hCMEC/D3 cells transfected with miR-155 inhibitor (Fig. 4*E*) partially reversed (by ~40%) the increase in paracellular permeability in hCMEC/D3 cells challenged with 1ng/ml of cytokines for 24h (Fig. 4*F*). These results indicate that miR-155 contributes to the cytokine-induced disruption of the paracellular seal of brain endothelium, which results in increased paracellular permeability to tracers *in vitro*.

Over-expression of miR-155 induces changes in the pattern of gene expression of hCMEC/D3 cells

To identify miR-155 target genes in BEC that might be implicated in BBB dysfunction relevant to human disease, we then analysed changes in mRNA expression of hCMEC/D3 cells that overexpress miR-155 using mRNA microarray analysis. We observed that 390 transcripts (of ~10,600 genes detected) were downregulated by at least ~1.2-fold with a $P < 0.01$ significant change by overexpression of miR-155 (GEO accession number GSE44694). Using clueGO (28) we observed that the three most statistically significant biological processes identified were translation ($P<0.01$), focal adhesion (FA) ($P<0.05$) and methionine metabolism ($P<0.05$) (Fig. 5*A*). Another bioinformatic analytical source, DAVID (29), further identified IJC ($P<0.05$) as a significantly enriched functional category among the miR-155-downregulated transcripts in hCMEC/D3 cells.

MiR-155 induces reorganization of focal adhesions and tight junctions in hCMEC/D3 cells

Since genes involved in FA were remarkably over represented in the set of genes downregulated by over expression of miR-155 in hCMEC/D3 cells, we investigated whether FA organization was affected by modulation of miR-155 levels using immunocytochemical techniques. Two structural components of FA, vinculin and talin, showed a characteristic staining pattern of FA, manifested by the presence of flat and elongated structures located centrally and near the cell periphery, in hCMEC/D3 cells transfected with scrambled pre-miR (Fig. 5*B*, 5*C*). In addition, vinculin immunostaining was also shown to be highly localised at the cell-cell junctions as shown by the belt-like staining pattern on the cell periphery (Fig. 5*B*).

Following transfection with pre-miR-155, vinculin immunostaining located centrally in hCMEC/D3 cells did not appear to be affected (Fig. 5*B*). However, we observed a remarkable reduction in the staining of vinculin located at the cell-cell junctions (Fig. 5*B*). Ectopic expression of miR-155 also altered talin sub-cellular distribution located centrally and at cell borders (Fig. 5*C*). TNFα and IFNγ-treatment induced a change in the cell morphology characterized by elongation of the cell shape accompanied by a reorganization of vinculin towards a more centrally localised and punctuate pattern (Fig. 5*B*). Inhibition of cytokine-induced increase in miR-155 levels by miR-155 inhibitor partially rescued vinculin (Fig. 5*B*), but not talin (Fig. 5*C*), delocalization at the cell-cell junctions.

We also observed that ZO-1 showed a continuous intercellular junction pattern at the cell borders in hCMEC/D3 cells transfected with scrambled pre-miR and in untransfected cells

(Fig. 5*D*). By contrast, over expressing miR-155 in BEC induced ZO-1 reorganization, characterized by disruption of its normal distribution from the cell-cell boundaries, similarly to the effect of cytokines on junctional organization (Fig. 5*D*). Furthermore, cytokine-induced redistribution of ZO-1 (Fig. 5*D*) was partially prevented by miR-155 inhibitor (Fig. 5*D*). Altogether, these results led us to investigate the putative target genes involved in miR-155-induced changes in FA and IJC organization that might contribute to alterations in the permeability of BEC.

Bioinformatic analysis and paracellular permeability assays identify four miR-155 putative targets associated with barrier dysfunction in hCMEC/D3 cells

Using TargetScan5.0 (8), we identified 63 putative target genes with a seed match for miR-155 that were downregulated by over expression of miR-155 at the mRNA level in hCMEC/D3 cells (Fig. 6*A,* Supplementary Table 1). In order to further select candidate genes associated with the increased paracellular permeability induced by miR-155 in BEC, we used additional criteria by only including genes associated with cell-cell junctions and/or the integrin adhesome (30-32) and those that were experimentally validated by 3'UTR reporter assays in other cell types (12, 13, 33). Using this strategy, we identified seven candidate genes including four components of FA, dedicator of cytokinesis 1 (DOCK-1), syntenin-1 (SDCBP), palladin (PALLD), integrin alpha-V (ITGAV) and three IJC molecules, annexin-2 (ANXA-2), claudin-1 (CLDN-1), and prion protein (PRNP) (Fig. 6*B*).

We then observed that reducing the expression of the FA components DOCK-1 and syntenin-1 induced a 1.4 fold increase in the paracellular permeability when compared with control (Fig. 7*A*). This effect was associated with delocalization of both ZO-1 and vinculin from the cell borders (Fig. 7*B*). Similarly, silencing claudin-1 and annexin-2 induced a 1.5 fold

increase in paracellular permeability when compared with controls (Fig. 7*A*). Silencing of claudin-1 also induced disassembly of ZO-1 from the cell borders (data not shown). Silencing of the remaining three candidate genes, palladin, integrin alpha-V and prion protein, did not induce an increase in the paracellular permeability of hCMEC/D3 cells (data not shown).

We next validated the regulatory roles of miR-155 in FA and IJC using luciferase reporter assay. Results showed that miR-155 overexpression in hCMEC/D3 cells decreased luciferase activity by approximately 30 to 40% in cells carrying 3'UTR of DOCK-1, syntenin-1, annexin-2 or claudin-1 when compared with scrambled pre-miR controls (Fig. 7*C*). These results were further supported by a decrease in the protein levels of DOCK-1 (~65%), syntenin-1 (~50%), annexin-2 (~30%) or claudin-1 (~50%) in hCMEC/D3 cells overexpressing miR-155 as evidenced by immunoblotting (Fig. 7*D*, 7*E*). These results demonstrate that four target genes for miR-155 including two components of FA, DOCK-1, syntenin-1, and two components of IJC, annexin-2 and claudin-1, modulate brain endothelial permeability and potentially mediate, at least partially, miR-155-induced BBB breakdown during inflammation.

Discussion

We propose that miR-155 acts as a novel negative regulator of BBB function during neuroinflammation by modulating brain endothelial cell-to-cell and cell-to-matrix interactions, thereby contributing to the pathogenesis of CNS neuroinflammatory disorders such as MS. The general consensus is that miR-155 is a proinflammatory miRNA (9) and that it might participate in the harmonization of cell activation during inflammatory processes in mammals. Consistent with this proposal, recent work has shown that miR-155 is highly expressed in active inflammatory MS plaques where astrocytes were identified as one of the potential cellular sources of this miRNA (15). Our results further suggest that miR-155 is highly expressed at the neurovascular unit during MS active lesion and is differentially upregulated in mouse whole spinal cords at different stages of EAE. Indeed, we used an animal model that show a reproducible and predictable relapsing-remitting EAE (20). During EAE-OS there is an infiltration of leucocytes and BBB leakage (20) without any significant changes in miR-155 levels in whole spinal cords. This suggests that the cellular source of miR-155 at this stage might be low and/or difficult to be detected if the increase in miR-155 is restricted to a few affected areas of the neurovascular unit. However, miR-155 levels are rapidly upregulated during paralysis in initial acute attack (APP) at a time when maximal cell infiltration is occurring around the vasculature (20). Furthermore, in this EAE model the recovery occurs when the animals begin to gain weight and clinical scores subside (20). This is accompanied by a gradual recovery of BBB function and reduction of cellular infiltration of the CNS (20), but we did not observe a decrease in the pro-inflammatory miR-155 levels. This result suggested that the proinflammatory cytokine profile at this stage was still high. It is tempting to speculate that activation mechanisms that initiate the resolution of the inflammatory response during the recovery phase might also be able to desensitize the neurovascular unit to the effects of miR-155, before any decrease in miR-155 levels are

observed by an unknown molecular mechanism. This may also be the case in the first remission phase when inflammatory lesions resolve and BBB dysfunction is minimal but miR-155 levels are still elevated (20). Another cellular sources of miR-155 in EAE spinal cords might be from activated leucocytes since mononuclear cells including T lymphocytes with increased miR-155 levels infiltrate the CNS parenchyma in EAE (10, 16). However, increased miR-155 levels at the neurovascular unit were observed in isolated microvessels of EAE spinal cords. We also observed by in situ hybridization that during neuroinflammation miR-155 appeared to be expressed in the microvasculature as well as in large blood vessels including venules.

Previous studies have shown that BBB breakdown is a fundamental event during the course of MS and that the magnitude of the neurovascular dysfunction in EAE is associated with the neurological severity of the disease (34). Furthermore, mice deficient in *bic/miR-155* gene showed partial resistance to develop EAE in this and previous studies (10, 16) and here we show that loss of miR-155 plays a protective role against BBB leakage at the region of inflammation. In addition, using LPS as an acute model of systemic inflammation with reduced leucocyte infiltration and circulating TNFα response, we observed that loss of miR-155 attenuated the increase of BBB permeability. However, these *in vivo* experiments are not conducive to unequivocally exclude the effect of miR-155 in other CNS resident cells, astrocytes and pericytes, during neurovascular inflammation. To test the hypothesis that brain endothelial miR-155 is involved in BBB dysfunction, we examined the effects of miR-155 on brain endothelial barrier functions in cell culture. Brain endothelial miR-155 is upregulated by proinflammatory cytokines in a time- and dose-dependent manner, an effect that coincides with cytokine-mediated brain endothelial barrier permeability (3). Moreover, our result show that ectopic expression of miR-155 mimicked cytokine-induced increase in permeability

whereas knockdown of endogenous miR-155 partially prevented cytokine-induced barrier disruption in BEC, indicating an active role for endothelial miR-155 in inflammation-induced BBB breakdown. Hence, miR-155 appears to be a pro-inflammatory miRNA, but it is induced by inflammation and/or infection at early times suggesting that it contributes to the early stages of inflammation at the neurovascular unit.

The mechanism by which miR-155 may exacerbate the breakdown of BBB appears to involve two different cellular pathways. First, miR-155 may be an important "control node" for the expression of IJC molecules in brain endothelium, thereby directly affecting the organization of cell-cell junctions. Consistent with our results Kong *et al.* reported that miR-155 induced delocalization of ZO-1 from the cell-cell contacts in tumorigenic epithelial cells (35). In this study, we identified that miR-155 may modulate BEC permeability and tight junction (TJ) organization, by directly targeting components of IJC, claudin-1 and annexin-2. Claudin-1, a target for miR-155, has an important barrier function at least in epithelial cells (36) although its expression by BEC *in vivo* is controversial (37). Recently, it has been shown that ectopic expression of claudin-1 in C57BL/6 mice prevents BBB leakiness in EAE animals as compared with littermate controls (32). Furthermore, loss of claudin-1 at the BBB has also been associated with barrier dysfunction in glioblastoma multiforme (38) and hepatitis C infection (39). In addition, annexin-2, another miR-155 target, has also been shown to regulate endothelial cell morphology and junctional integrity via its association with VE-cadherin (31). However, little is known about the contribution of annexin-2 to strengthening the BEC barrier. Here we have shown that silencing of annexin-2 expression has significant consequences for BEC barrier function at least *in vitro*. Hence, miR-155 direct targeting of at least two components of CNS interendothelial junctional complexes may lead to increased BBB permeability.

A second cellular pathway modulated by endothelial miR-155 involves FA organization, which may also lead to increased BBB permeability following a cytokine stimulus. We observed that miR-155 affects the distribution of vinculin and talin in BEC suggesting alterations in the cellular attachment to their matrix substrate. Vinculin is a cytoskeleton-associated protein and plays an important role in FA assembly and strength (40). Talin, another FA molecule, directly interacts with the cytoplasmic tail of ß-integrins inducing their activation (41). Indeed, β1-integrin-mediated adhesion of BEC to the surrounding ECM has been recently shown to be critical for stabilizing claudin-5 in tight junctions and for BBB integrity (42). Here, we observed that miR-155 has the capacity to directly target FA components in BEC and that downregulation of at least some of these components may lead to increased BEC permeability. For instance, DOCK-1 forms part of focal contacts and participates in the downstream integrin signal transduction pathway by forming complexes with engulfment and cell motility (ELMO) protein (43). It is possible that the DOCK-1-ELMO complex, a guanine nucleotide exchange factor, might regulate endothelial permeability by modulating the activity of Rho-family GTPases such as Rac-1 although this does not exclude the possibility that FA disassembly may directly lead to increased BEC permeability (44). Indeed, another focal adhesion molecule that we found to be regulated by miR-155 in cultured BEC is syntenin-1, an adaptor and scaffold protein that contains PDZ (postsynaptic density protein-95, postsynaptic discs large, and zona occludens-1) motifs. Initially, syntenin-1 was shown to interact with syndecans, heparan sulfate proteoglycans that assist cell adhesion and promote attraction and concentration of growth factors at the cell surface (45). It has also been shown that knockdown of syntenin-1 prevents fibronectin-induced formation of integrin ß1/FAK/c-Src complex, which may play an important role in the downstream focal contact signalling pathway (46). Therefore, it appears that not only

structural FA proteins are important for stabilizing TJs and the brain endothelial barrier but also FA adaptor and signaling proteins. While in other cell types such as fibroblasts (47), miR-155 may promote migration by silencing genes implicated in modulating cell-to-matrix attachment, endothelial miR-155 may indirectly contribute to increased BBB permeability via targeting FA components.

In conclusion, we propose that miR-155 modulates key features of the brain endothelial barrier during inflammation and might play an important role during the pathogenesis of CNS inflammatory disorders that affect BBB. In addition, endothelial miR-155 may be acts as an effector of inflammatory mediators associated with promotion of inflammation and subsequent barrier breakdown. Here we demonstrate that miR-155 might contribute to BBB breakdown during neuroinflammation by altering the phenotype and function of neurovascular endothelium, in particular components of cell-to-cell and cell-to-matrix adhesion pathways, thereby revealing potential therapeutic targets to ameliorate for CNS inflammatory disorders.

Acknowledgments:

This work was funded by the Multiple Sclerosis Society of Great Britain and Northern Ireland. The authors are grateful to Julia Barkans for general laboratory infrastructure assistance, Jacky Brown, Payam Rezaie for preparation of MS samples for histological characterization, Rachel Waller for preparation of samples for LCM. Catherine Hare and Caitriona O'Rourke for reviewing the manuscript. Tissue samples and associated clinical and neuropathological data were supplied by the UK MS Tissue Bank.

References

1. Lopez-Ramirez, M. A., Male, D. K., Wang, C., Sharrack, B., Wu, D., and Romero, I. A. (2013) Cytokine-induced changes in the gene expression profile of a human cerebral microvascular endothelial cell-line, hCMEC/D3. *Fluids and barriers of the CNS* **10**, 27
2. Schlegel, N., and Waschke, J. (2009) Impaired integrin-mediated adhesion contributes to reduced barrier properties in VASP-deficient microvascular endothelium. *J Cell Physiol* **220**, 357-366
3. Lopez-Ramirez, M. A., Fischer, R., Torres-Badillo, C. C., Davies, H. A., Logan, K., Pfizenmaier, K., Male, D. K., Sharrack, B., and Romero, I. A. (2012) Role of Caspases in Cytokine-Induced Barrier Breakdown in Human Brain Endothelial Cells. *J Immunol* **189**, 3130-3139
4. Mankertz, J., Tavalali, S., Schmitz, H., Mankertz, A., Riecken, E., Fromm, M., and Schulzke, J. (2000) Expression from the human occludin promoter is affected by tumor necrosis factor alpha and interferon gamma. *J. Cell Sci.* **113**, 2085-2090
5. Forster, C., Burek, M., Romero, I. A., Weksler, B., Couraud, P. O., and Drenckhahn, D. (2008) Differential effects of hydrocortisone and TNFalpha on tight junction proteins in an in vitro model of the human blood-brain barrier. *J Physiol* **586**, 1937-1949
6. Murakami, T., Felinski, E. A., and Antonetti, D. A. (2009) Occludin Phosphorylation and Ubiquitination Regulate Tight Junction Trafficking and Vascular Endothelial Growth Factor-induced Permeability. *J. Biol. Chem.* **284**, 21036-21046
7. Reijerkerk, A., Lopez-Ramirez, M. A., Bert van het Hof, Joost A.R. Drexhage, Wouter Kamphuis, Kooij, G., Joost B. Vos, Tineke C.T.M van der Pouw Kraan, Anton J. van Zonneveld, Horrevoets, A. J., Prat, A., Romero, I. A., and de Vries, H. E. (2013) microRNAs regulate human brain endothelial cell barrier function in inflammation: implications for multiple sclerosis. *Journal of Neuroscience* **17,** 6857-6863
8. Friedman, R. C., Farh, K. K.-H., Burge, C. B., and Bartel, D. P. (2009) Most mammalian mRNAs are conserved targets of microRNAs. *Genome Res.* **19**, 92-105
9. Baltimore, D., Boldin, M., O'Connell, R., Rao, D., and Taganov, K. (2008) MicroRNAs: new regulators of immune cell development and function. *Nat Immunol* **9**, 839-845
10. O'Connell, R. M., Kahn, D., Gibson, W. S., Round, J. L., Scholz, R. L., Chaudhuri, A. A., Kahn, M. E., Rao, D. S., and Baltimore, D. (2010) MicroRNA-155 promotes autoimmune inflammation by enhancing inflammatory T cell development. *Immunity* **33**, 607-619
11. Kong, W., Yang, H., He, L., Zhao, J.-j., Coppola, D., Dalton, W. S., and Cheng, J. Q. (2008) MicroRNA-155 Is Regulated by the Transforming Growth Factor {beta}/Smad Pathway and Contributes to Epithelial Cell Plasticity by Targeting RhoA. *Mol. Cell. Biol.* **28**, 6773-6784
12. Guo, H., Ingolia, N. T., Weissman, J. S., and Bartel, D. P. (2010) Mammalian microRNAs predominantly act to decrease target mRNA levels. *Nature* **466**, 835-840
13. Selbach, M., Schwanhausser, B., Thierfelder, N., Fang, Z., Khanin, R., and Rajewsky, N. (2008) Widespread changes in protein synthesis induced by microRNAs. *Nature* **455**, 58-63
14. Sun, H. X., Zeng, D. Y., Li, R. T., Pang, R. P., Yang, H., Hu, Y. L., Zhang, Q., Jiang, Y., Huang, L. Y., Tang, Y. B., Yan, G. J., and Zhou, J. G. (2012) Essential role of

microRNA-155 in regulating endothelium-dependent vasorelaxation by targeting endothelial nitric oxide synthase. *Hypertension* **60**, 1407-1414
15. Junker, A., Krumbholz, M., Eisele, S., Mohan, H., Augstein, F., Bittner, R., Lassmann, H., Wekerle, H., Hohlfeld, R., and Meinl, E. (2009) MicroRNA profiling of multiple sclerosis lesions identifies modulators of the regulatory protein CD47. *Brain* **132**, 3342-3352
16. Murugaiyan, G., Beynon, V., Mittal, A., Joller, N., and Weiner, H. L. (2011) Silencing microRNA-155 ameliorates experimental autoimmune encephalomyelitis. *J Immunol* **187**, 2213-2221
17. Yao, R., Ma, Y. L., Liang, W., Li, H. H., Ma, Z. J., Yu, X., and Liao, Y. H. (2012) MicroRNA-155 modulates Treg and Th17 cells differentiation and Th17 cell function by targeting SOCS1. *PloS one* **7**, e46082
18. O'Connell, R. M., Taganov, K. D., Boldin, M. P., Cheng, G., and Baltimore, D. (2007) MicroRNA-155 is induced during the macrophage inflammatory response. *PNAS* **104**, 1604-1609
19. Dunand-Sauthier, I., Santiago-Raber, M. L., Capponi, L., Vejnar, C. E., Schaad, O., Irla, M., Seguin-Estevez, Q., Descombes, P., Zdobnov, E. M., Acha-Orbea, H., and Reith, W. (2011) Silencing of c-Fos expression by microRNA-155 is critical for dendritic cell maturation and function. *Blood* **117**, 4490-4500
20. Al-Izki, S., Pryce, G., Jackson, S. J., Giovannoni, G., and Baker, D. (2012) Immunosuppression with FTY720 is insufficient to prevent secondary progressive neurodegeneration in experimental autoimmune encephalomyelitis. *Multiple Sclerosis Journal* **17**, 939-948
21. Simpson, J. E., Ince, P. G., Shaw, P. J., Heath, P. R., Raman, R., Garwood, C. J., Gelsthorpe, C., Baxter, L., Forster, G., Matthews, F. E., Brayne, C., and Wharton, S. B. (2011) Microarray analysis of the astrocyte transcriptome in the aging brain: relationship to Alzheimer's pathology and APOE genotype. *Neurobiol Aging* **32**, 1795-1807
22. Abbott, N. J., Hughes, C. C., Revest, P. A., and Greenwood, J. (1992) Development and characterisation of a rat brain capillary endothelial culture: towards an in vitro blood-brain barrier. *Journal of cell science* **103 (Pt 1)**, 23-37
23. Livak, K. J., and Schmittgen, T. D. (2001) Analysis of Relative Gene Expression Data Using Real-Time Quantitative PCR and the 2-[Delta][Delta]CT Method. *Methods* **25**, 402-408
24. Obernosterer, G., Martinez, J., and Alenius, M. (2007) Locked nucleic acid-based in situ detection of microRNAs in mouse tissue sections. *Nature protocols* **2**, 1508-1514
25. Hoffmann, A., Bredno, J., Wendland, M., Derugin, N., Ohara, P., and Wintermark, M. (2011) High and Low Molecular Weight Fluorescein Isothiocyanate (FITC)-Dextrans to Assess Blood-Brain Barrier Disruption: Technical Considerations. *Transl Stroke Res* **2**, 106-111
26. Manaenko, A., Chen, H., Kammer, J., Zhang, J. H., and Tang, J. (2011) Comparison Evans Blue injection routes: Intravenous versus intraperitoneal, for measurement of bloodâ€“brain barrier in a mice hemorrhage model. *Journal of Neuroscience Methods* **195**, 206-210
27. Rodriguez, A., Vigorito, E., Clare, S., Warren, M. V., Couttet, P., Soond, D. R., van Dongen, S., Grocock, R. J., Das, P. P., Miska, E. A., Vetrie, D., Okkenhaug, K., Enright, A. J., Dougan, G., Turner, M., and Bradley, A. (2007) Requirement of bic/microRNA-155 for normal immune function. *Science* **316**, 608-611
28. Bindea, G., Mlecnik, B., Hackl, H., Charoentong, P., Tosolini, M., Kirilovsky, A., Fridman, W.-H., PagÃ¨s, F., Trajanoski, Z., and Galon, J. r. m. (2009) ClueGO: a

Cytoscape plug-in to decipher functionally grouped gene ontology and pathway annotation networks. *Bioinformatics* **25**, 1091-1093
29. Huang, D. W., Sherman, B. T., and Lempicki, R. A. (2008) Systematic and integrative analysis of large gene lists using DAVID bioinformatics resources. *Nat. Protocols* **4**, 44-57
30. Zaidel-Bar, R., Itzkovitz, S., Ma'ayan, A., Iyengar, R., and Geiger, B. (2007) Functional atlas of the integrin adhesome. *Nat Cell Biol* **9**, 858-867
31. Su, S.-C., Maxwell, S. A., and Bayless, K. J. (2010) Annexin 2 Regulates Endothelial Morphogenesis by Controlling AKT Activation and Junctional Integrity. *J. Biol. Chem.* **285**, 40624-40634
32. Pfeiffer, F., Schafer, J., Lyck, R., Makrides, V., Brunner, S., Schaeren-Wiemers, N., Deutsch, U., and Engelhardt, B. (2011) Claudin-1 induced sealing of blood-brain barrier tight junctions ameliorates chronic experimental autoimmune encephalomyelitis. *Acta Neuropathol* **122**, 601-614
33. Xu, G., Fewell, C., Taylor, C., Deng, N., Hedges, D., Wang, X., Zhang, K., Lacey, M., Zhang, H., Yin, Q., Cameron, J., Lin, Z., Zhu, D., and Flemington, E. K. (2010) Transcriptome and targetome analysis in MIR155 expressing cells using RNA-seq. *RNA* **16**, 1610-1622
34. Fabis, M. J., Phares, T. W., Kean, R. B., Koprowski, H., and Hooper, D. C. (2008) Blood-brain barrier changes and cell invasion differ between therapeutic immune clearance of neurotrophic virus and CNS autoimmunity. *PNAS* **105**, 15511-15516
35. Kong, W., He, L., Coppola, M., Guo, J., Esposito, N. N., Coppola, D., and Cheng, J. Q. (2008) MicroRNA-155 regulates cell survival, growth, and chemosensitivity by targeting FOXO3a in breast cancer. *J Biol Chem* **285**, 17869-17879
36. Inai, T., Kobayashi, J., and Shibata, Y. (1999) Claudin-1 contributes to the epithelial barrier function in MDCK cells. *Eur J Cell Biol* **78**, 849-855
37. Wolburg, H., Wolburg-Buchholz, K., Kraus, J., Rascher-Eggstein, G., Liebner, S., Hamm, S., Duffner, F., Grote, E.-H., Risau, W., and Engelhardt, B. (2003) Localization of claudin-3 in tight junctions of the blood-brain barrier is selectively lost during experimental autoimmune encephalomyelitis and human glioblastoma multiforme. *Acta Neuropathologica* **105**, 586-592
38. Liebner, S., Fischmann, A., Rascher, G., Duffner, F., Grote, E., Kalbacher, H., and Wolburg, H. (2000) Claudin-1 and claudin-5 expression and tight junction morphology are altered in blood vessels of human glioblastoma multiforme. *Acta Neuropathol* **100**, 323-331
39. Fletcher, N. F., Wilson, G. K., Murray, J., Hu, K., Lewis, A., Reynolds, G. M., Stamataki, Z., Meredith, L. W., Rowe, I. A., Luo, G., Lopez-Ramirez, M. A., Baumert, T. F., Weksler, B., Couraud, P. O., Kim, K. S., Romero, I. A., Jopling, C., Morgello, S., Balfe, P., and McKeating, J. A. (2012) Hepatitis C Virus Infects the Endothelial Cells of the Blood-Brain Barrier. *Gastroenterology* **142**, 634-643
40. Ziegler, W. H., Gingras, A. R., Critchley, D. R., and Emsley, J. (2008) Integrin connections to the cytoskeleton through talin and vinculin. *Biochem Soc Trans* **36**, 235-239
41. Nayal, A., Webb, D. J., and Horwitz, A. F. (2004) Talin: an emerging focal point of adhesion dynamics. *Curr Opin Cell Biol* **16**, 94-98
42. Osada, T., Gu, Y. H., Kanazawa, M., Tsubota, Y., Hawkins, B. T., Spatz, M., Milner, R., and Del Zoppo, G. J. (2011) Interendothelial claudin-5 expression depends on cerebral endothelial cell-matrix adhesion by beta(1)-integrins. *J Cereb Blood Flow Metab* **31**, 1972-1985

43. Komander, D., Patel, M., Laurin, M. l., Fradet, N., Pelletier, A., Barford, D., and Cote JF (2008) An alpha-Helical Extension of the ELMO1 Pleckstrin Homology Domain Mediates Direct Interaction to DOCK180 and Is Critical in Rac Signaling. *Molecular Biology of the Cell* **19**, 4837-4851
44. Epting, D., Wendik, B., Bennewitz, K., Dietz, C. T., Driever, W., and Kroll, J. (2010) The Rac1 regulator ELMO1 controls vascular morphogenesis in zebrafish. *Circ Res* **107**, 45-55
45. Beekman, J. M., and Coffer, P. J. (2008) The ins and outs of syntenin, a multifunctional intracellular adaptor protein. *Journal of cell science* **121**, 1349-1355
46. Hwangbo, C., Kim, J., Lee, J. J., and Lee, J. H. (2010) Activation of the integrin effector kinase focal adhesion kinase in cancer cells is regulated by crosstalk between protein kinase Calpha and the PDZ adapter protein mda-9/Syntenin. *Cancer Res* **70**, 1645-1655
47. Pottier, N., Maurin, T., Chevalier, B., Puissagur, M.-P., Lebrigand, K., Robbe-Sermesant, K., Bertero, T., Lino Cardenas, C. L., Courcot, E., Rios, G. r., Fourre, S., Lo-Guidice, J.-M., Marcet, B., Cardinaud, B., Barbry, P., and Mari, B. (2009) Identification of Keratinocyte Growth Factor as a Target of microRNA-155 in Lung Fibroblasts: Implication in Epithelial-Mesenchymal Interactions. *PloS one* **4**, e6718

Figure legends

Figure 1. MiR-155 is induced in active lesions of MS patients. ***A***, Demographic and clinical characteristics of MS and control brain samples used in the study. NA= not applicable, NIA= no information available. ***B***, Laser capture microdissection was used to isolate cerebral blood vessels from active lesions of multiple sclerosis patients (MS-AL) and normal appearing white matter of MS patients (MS-NAWM), and total RNA was then extracted. MiR-155 expression levels were determined by quantitative RT-PCR. U6B small nuclear RNA was used as an internal standard.

Figure 2. MiR-155 is induced in spinal cords of EAE mice. ***A***, EAE was induced in Biozzi ABH mice using spinal cord homogenates, and total RNA from spinal cords at different clinical status (OS, onset of signs; APP, acute phase paralysis; Recovery; Remission; Chronic) were used to determine levels of miR-155 by quantitative RT-PCR. U6B small nuclear RNA was used as an internal standard. **P*<0.05, ***P*<0.01, ****P*<0.001 compared to their normal littermate controls (n=6). ***B***, Total RNA from isolated spinal cord microvessels in EAE APP mice and in their control littermates were used to determine miR-155 levels by quantitative RT-PCR. Microvessels from the spinal cord of 3 mice were pooled and analyzed as one sample. Data represent the mean ± SEM, ***P*<0.01, compared to their normal littermate controls (n=3). ***C,*** Total RNA in *B* were used to determine brain endothelial cell (*claudin-5 and pecam-1*), astrocytes (*gfap*) and leucocyte (*cd-45*) markers by quantitative RT-PCR. ***D*** and ***E***, hematoxylin and eosin staining of a spinal cord from EAE APP mice. Immune-cell infiltration is illustrated at higher magnification in *E*. Scales bar in *D* is 500 μm and in *E* is 50 μm. ***F***, ***G*** and ***H***, *In situ* hybridization for miR-155 combined with immunohistochemistry to identify PECAM-1+ cells in EAE mouse spinal cord. (*F*) In the bottom left panel, DAPI labels nuclei and a white arrow shows nucleus of a brain endothelial

cell. The upper left panel shows expression of miR-155 (black arrow) and a higher magnification is shown in ***G***. The bottom right panel shows immunostaining of the endothelial specific marker PECAM-1 (white arrow). A merged image (upper right panel) demonstrates co-localization of miR-155 and PECAM-1 (black arrows) and a higher magnification is shown in ***H***. APP, EAE ABH mouse at acute stage with a clinical score of 4. Scale bar, 25μm.

Figure 3. Inflammation-induced BBB breakdown is partially prevented in miR-155$^{-/-}$ mice. EAE was induced in miR-155$^{+/+}$ and miR-155$^{-/-}$ mice using Hooke Kit™ MOG_{35-55}/CFA Emulsion PTX. ***A***, Deletion of miR-155 ameliorates EAE. * Two way ANOVA test of clinical score of all the time points demonstrated significant difference between the two groups. Data presented as mean ± SEM (n = 10 for each group). ***B***, At day 21 after induction, mice were injected intravenously with 70kDa FITC-dextran (250mg/kg), and lumbar spinal cords and livers were taken after perfusion with fixative. Images of cross sections of spinal cords at lumbar 4-5 levels were analyzed to determine extravascular fluorescence intensity. (***B***) Representative images show control non-immunized miR-155$^{+/+}$ and miR-155$^{-/-}$ mice, or immunized miR155$^{+/+}$ and miR-155$^{-/-}$ EAE mice. Scale bar, 25μm. ***C***, Quantification of extravascular intensity of 70kDa FITC-dextran. For each mouse, the fluorescence intensity of spinal cord sections was normalized to that of liver sections from the same animal. *P<0.05 compared with non-immunized miR-155$^{+/+}$ and miR-155$^{-/-}$ mice or immunized miR-155$^{-/-}$ EAE mice by ANOVA with post-hoc comparisons and Tukey HSD correction. Error bars represent SEM (n=10). ***D***, Plasma levels of TNFα in WT and miR-155$^{-/-}$ mice 6 h after intraperitoneal injection of LPS (4mg/kg) assessed by ELISA. Values are represented as fold change of LPS-treated WT and LPS-treated miR-155$^{-/-}$ mice relative to those in PBS-treated WT (5.03±0.85pg/ml) and PBS-treated miR-155$^{-/-}$ (4.21±0.37pg/ml), respectively. Error bars

represent SEM (n=4 for PBS group, n=6 for LPS group). ***E***, Quantification of efflux of Evans blue in the spinal cords of mice as in *D*. **P*<0.05 compared with PBS (vehicle) injected miR-155$^{+/+}$ and miR-155$^{-/-}$ mice or with LPS injected miR-155$^{-/-}$ mice by ANOVA with post-hoc comparisons and Tukey HSD correction. Error bars represent SEM (n=4 for PBS group, n=6 for LPS group).

Figure 4. MiR-155 contributes to cytokine-induced brain endothelial barrier breakdown *in vitro*. ***A***, Total RNA was isolated from hCMEC/D3 cells treated with TNFα and IFNγ or TNFα and IL1β or IL1β and IFNγ to determine miR-155 levels by quantitative RT-PCR. MiR-24 is an example of miRNA that did not change following cytokines treatment. U6B small nuclear RNA was used as an internal standard. Data represent the mean ± SEM, ***P*<0.01 compared to unstimulated cells (n=3). ***B***, Confluent monolayers of hCMEC/D3 cells were stimulated with TNFα and IFNγ at 1, 10 and 100 ng/ml for 24 h or treated with TNFα and IFNγ (100ng/ml) at 2, 6 and 24h to determine miR-155 levels by quantitative RT-PCR. Control values were normalized to one and results are expressed as miRNA levels in TNFα and IFNγ-treated cells relative to those in unstimulated cells. Data represent the mean ± SEM, **P*<0.05, ***P*<0.01 compared to unstimulated cells (n=3). ***C***, MiR-155 expression levels in hCMEC/D3 cells treated with TNFα and IFNγ (1ng/ml) or transfected with pre-miR-155 (30nM) for 24 h. Values are represented as miRNA levels relative to those in control cells or in cells transfected with scrambled pre-miR, respectively. U6B small nuclear RNA was used as an internal standard. $^{*,\#}$*P*<0.05 compared to *vehicle or $^{\#}$scrambled pre-miR transfected cells, respectively. Data represent the mean ± SEM (n=3). ***D***, The brain endothelial permeability coefficient (Pe) for 70kDa FITC dextran was measured in cells transfected with pre-miR-155 or stimulated with TNFα and IFNγ as in *C*. Data represent the mean ± SEM and $^{*,\#}$*P*<0.05 compared to *vehicle or $^{\#}$scrambled pre-miR transfected cells,

respectively (n=3). ***E***, MiR-155 levels were analyzed in hCMEC /D3 cells transfected with scrambled miR inhibitor (60nM) or miR-155 inhibitor (60nM) in the presence and absence of TNFα and IFNγ (1ng/ml) for 24 h. U6B RNA was used as an internal standard. Data represent the mean ± SEM (n=3). $^{\#}P<0.05$ compared to scrambled miR inhibitor-transfected cells. ***F***, Permeability coefficient (Pe) for 70kDa FITC dextran was measured in hCMEC /D3 cells transfected with scrambled miR inhibitor or miR-155 inhibitor in the presence and absence of TNFα and IFNγ as in *E*. Data represent the mean ± SEM and $^{*,\#}P<0.05$ compared to *basal scrambled miR inhibitor-transfected cells. or $^{\#}$cytokine-treated scrambled miR inhibitor-transfected cells (n=3).

Figure 5. MiR-155 induces changes in the pattern of gene expression of junctional molecules in hCMEC/D3 cells and alters their subcellular distribution. ***A***, A list of genes with downregulated mRNA transcripts following ectopic expression of miR-155 in hCMEC/D3 cells, determined by microarray analysis, was used to create a pie visualization map with KEGG, Biocarta and GO molecular functions by the ClueGO bioinformatic tool (28) (The full data analysis of mRNA transcripts altered by overexpression of miR-155 in hCMEC/D3 cells can be accessed in GEO with accession number GSE44694). ***B, C*** and ***D***, hCMEC/D3 cells were transfected with either pre-miR-155, or miR-155 inhibitor prior to addition of TNFα and IFNγ (1ng/ml) for 24h. (***B***) Vinculin and (***C***) talin were used as focal adhesion markers and visualized by immunofluorescence. In untransfected or scrambled pre-miR-transfected hCMEC/D3 cells, vinculin and talin staining pattern was located centrally and at the cell borders. Over expression of miR-155 induced the disappearance of vinculin primarily from the cell borders whereas talin was delocalized both from the cell borders and centrally. TNFα and IFNγ induced reorganization of both vinculin and talin in hCMEC/D3 cells, but only vinculin delocalization was partially prevented by miR-155 inhibitor. Images are

representative of three separate experiments. Scale bar, 20µm. (***D***) Arrow heads show ZO-1 immunostaining in hCMEC/D3 cells characteristic of TJs discerned by continuous staining at the cell borders (arrowheads). The arrows show that miR-155 overexpression or TNFα and IFNγ stimulus for 24h induced ZO-1 fragmentation from the cell to cell contacts compared with cells transfected with scrambled pre-miR or treated with vehicle. Knockdown of miR-155 using miR-155 inhibitor partially prevented cytokine-induced disassembly of ZO-1 as indicated by arrowheads (Bottom right). Images are representative of four separate experiments. Scale bars, 25µm.

Figure 6. MiR-155 predicted targets in hCMEC/D3 cells. hCMEC/D3 cells were transfected with pre-miR-155 or with scrambled pre-miR as a control. RNA was extracted and analyzed using microarray profiling. hCMEC/D3 cells expressed ~10,600 genes out of ~24,000 genes tested. ***A***, Two-way Venn diagram of genes downregulated by ectopic expression of miR-155 and putative predicted targets for miR-155 expressed by hCMEC/D3 cells. Sixty three genes where identified to have target sites for miR-155 and downregulated after ectopic expression of miR-155 in hCMEC/D3 cells. ***B***, Table showing seven candidate genes involved in miR-155-induced barrier breakdown in hCMEC/D3 cells. Criteria for selection: 1) Genes downregulated at the mRNA levels by ectopic expression of miR-155 (The full data analysis of mRNA transcripts altered by overexpression of miR-155 in hCMEC/D3 cells can be accessed in GEO with accession number GSE44694); 2) Genes with function related to cell-cell or cell-matrix adhesion; 3) miR-155 predicted targets as identified by databases (Targetscan) and/or experimentally validated by 3' UTR-reporter assays in other cell types (12, 13, 33).

Figure 7. MiR-155 silences genes associated with cell-cell and cell-matrix junctions leading to increased paracellular permeability in hCMEC/D3 cells. ***A***, Silencing of DOCK-1, syntenin-1, annexin-2 or claudin-1 using specific siRNAs induced an increase in hCMEC/D3 cells paracellular permeability to FITC-dextran. **P*<0.05, ***P*<0.01 compared to non-target siRNA negative control. Error bars represent SEM (n=3 or 4). *B*, Silencing of DOCK-1 or syntenin-1 using specific siRNAs induced delocalization of ZO-1 and vinculin from the cell periphery denoted by arrows. Images are representative of three separate experiments. Scale bar, 20μm. ***C***, Cells were transiently transfected with pre-miR-155 or scrambled pre-miR in hCMEC/D3 cells stably expressing luciferase constructs with the 3' UTR of the indicated genes. Ectopic expression of miR-155 reduces luciferase activity for each construct. Data represente mean ± SEM (n=3). **P*<0.05 compared to scrambled pre-miR-transfected cells. ***D***, DOCK-1, syntenin-1, annexin-2 and claudin-1 protein levels were determined using Western blot analysis in hCMEC/D3 cells transfected with scrambled pre-miR or pre-miR-155. The same blots were reprobed with anti-actin antibody as indicated for each gene. ***E***, Protein expression levels in *D* were quantified using ImageJ software and presented as mean ± SEM (n=3). **P*<0.05 compared to scrambled pre-miR-transfected cells.

Figure 1

A

Patient	Age/ Gender	Post mortem	Type of MS	Disease duration	Lesion activity	Cause of death
M1	54/F	22 h	Secundary progressive	Unknown	CAL/CL	Broncopneumonia
M2	75/M	22 h	Secundary progressive	32 years	CAL/CL	Pneumonia
M3	53/M	13 h	Secundary progressive	16 years	CAL	Pneumonia
M4	34/F	12 h	Secundary progressive	Unknown	AL/CAL/CL	Pneumonia
M5	88/F	22 h	Primary progressive	30 years	AL/CAL	Broncopneumonia
M6	72/F	8 h	Relap-remit to Sec-prog	41 years	AL/CAL/CL	Broncopneumonia
C1	73/M	21 h	Control	NA	NA	Cardiogenic shock
C2	64/M	18 h	Control	NA	NA	Cardiac failure
C3	82/M	21 h	Control	NA	NA	Natural death
C4	35/M	22 h	Control	NA	NA	Cancer tongue
C5	84/M	5 h	Control	NA	NA	Bladder cancer
C6	82/M	21 h	Control	NA	NA	Rheumatoid Arthritis

B

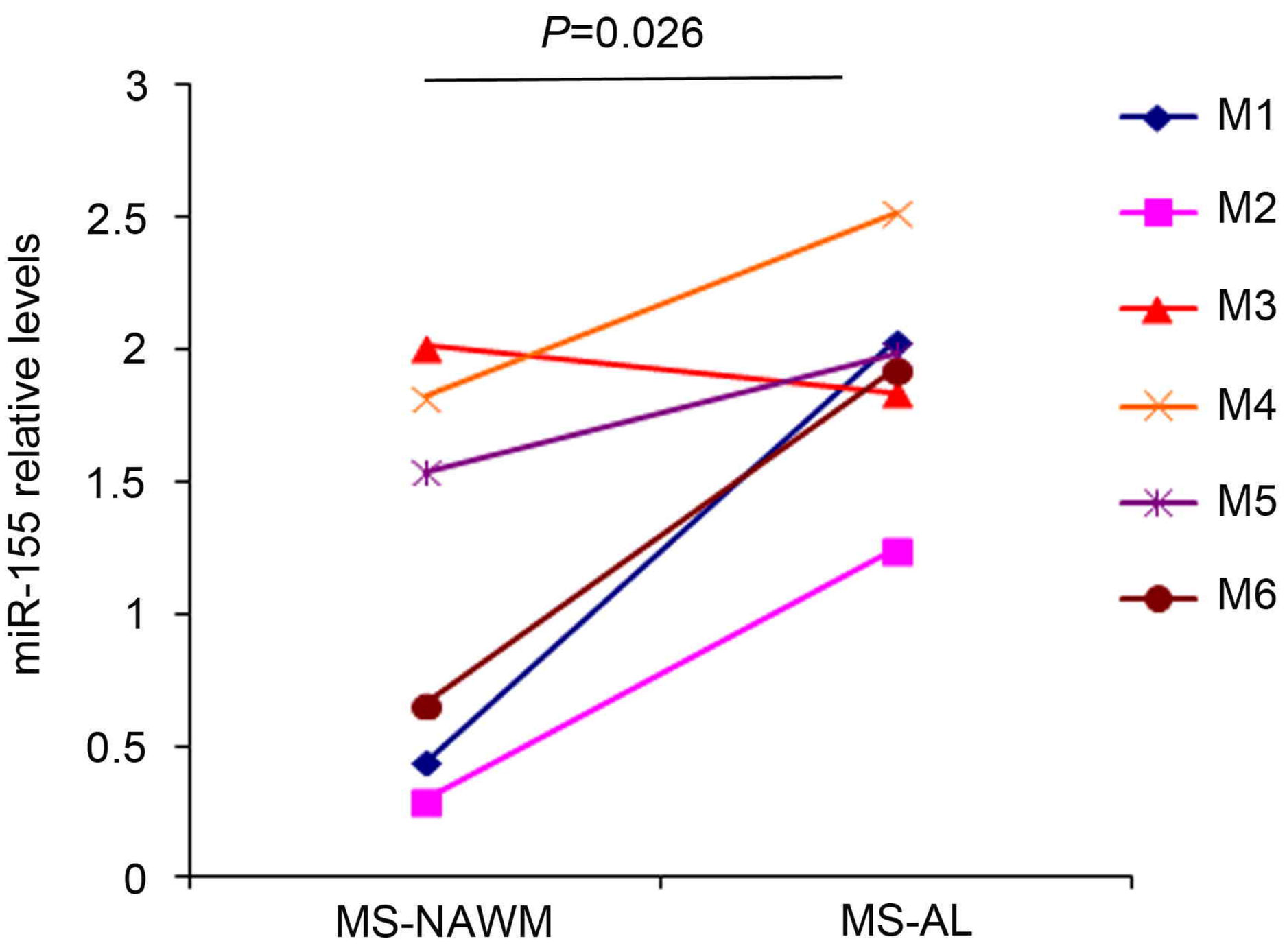

Figure 2

A

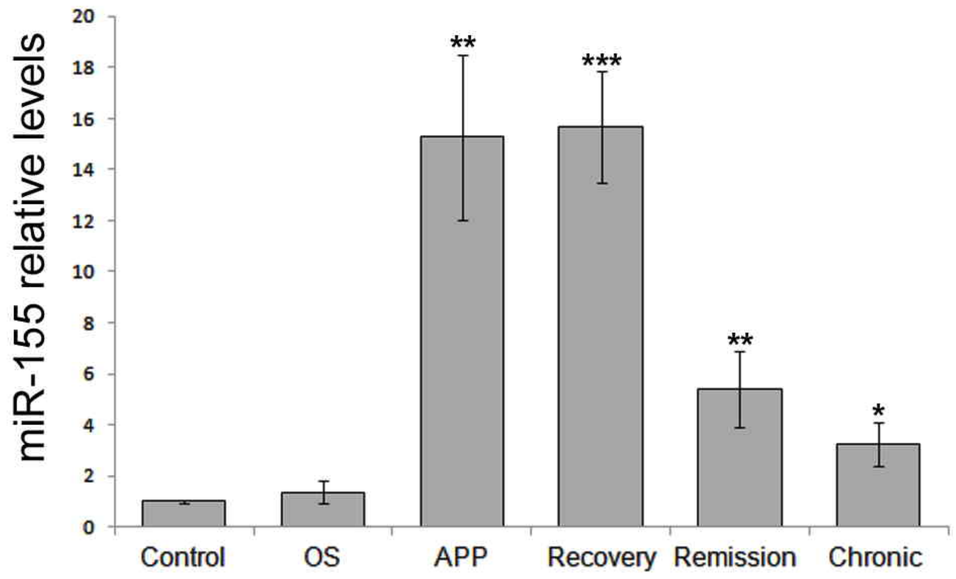

B

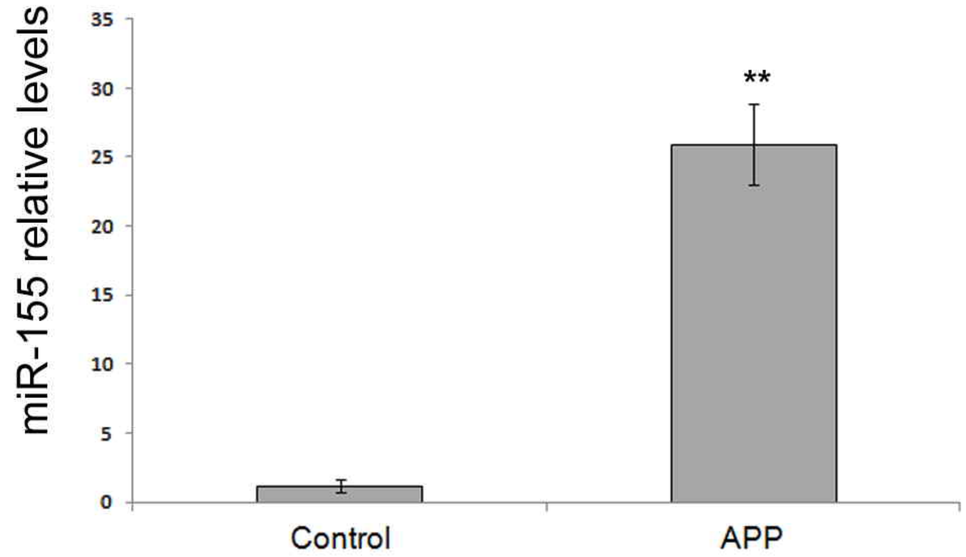

C

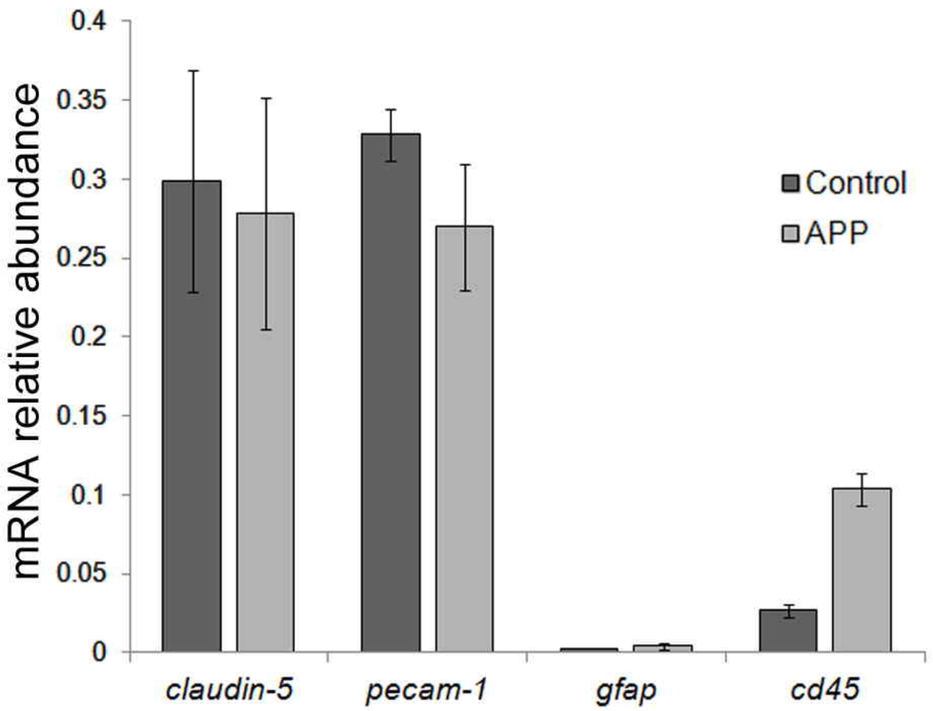

D

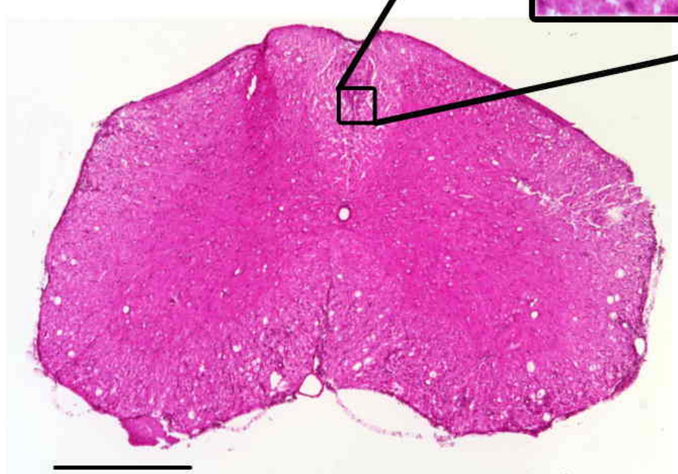

E

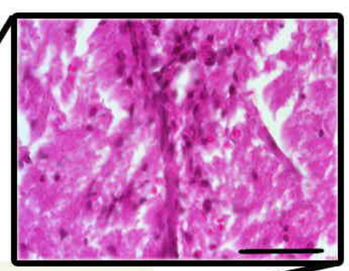

F

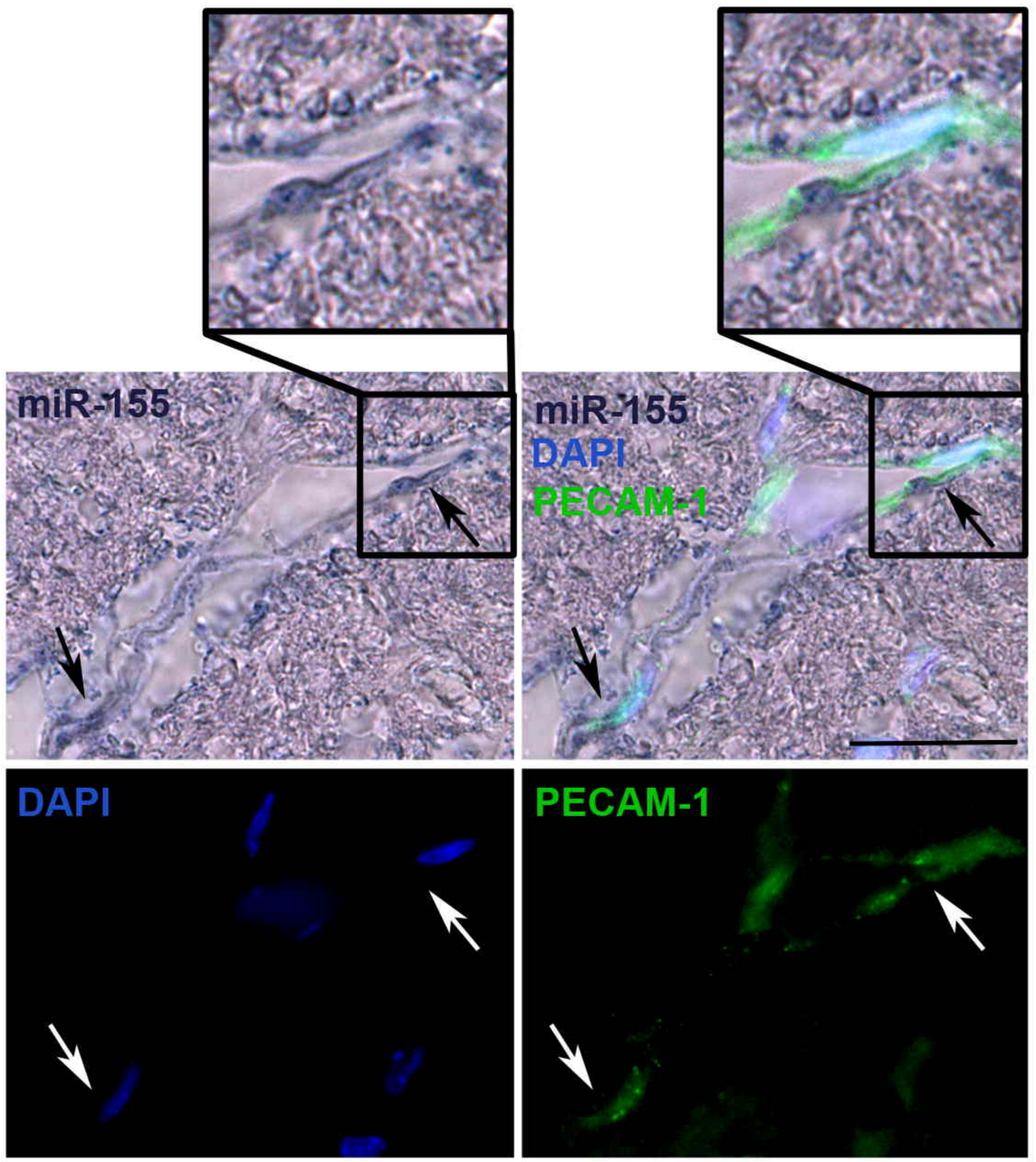

G

H

Figure 3

A

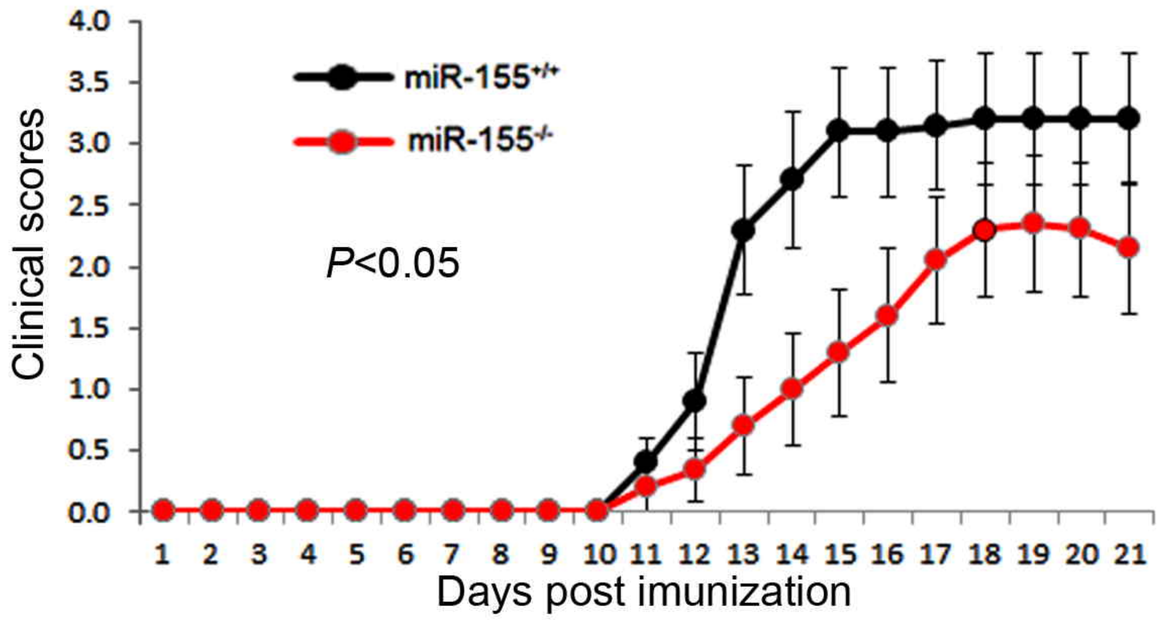

B

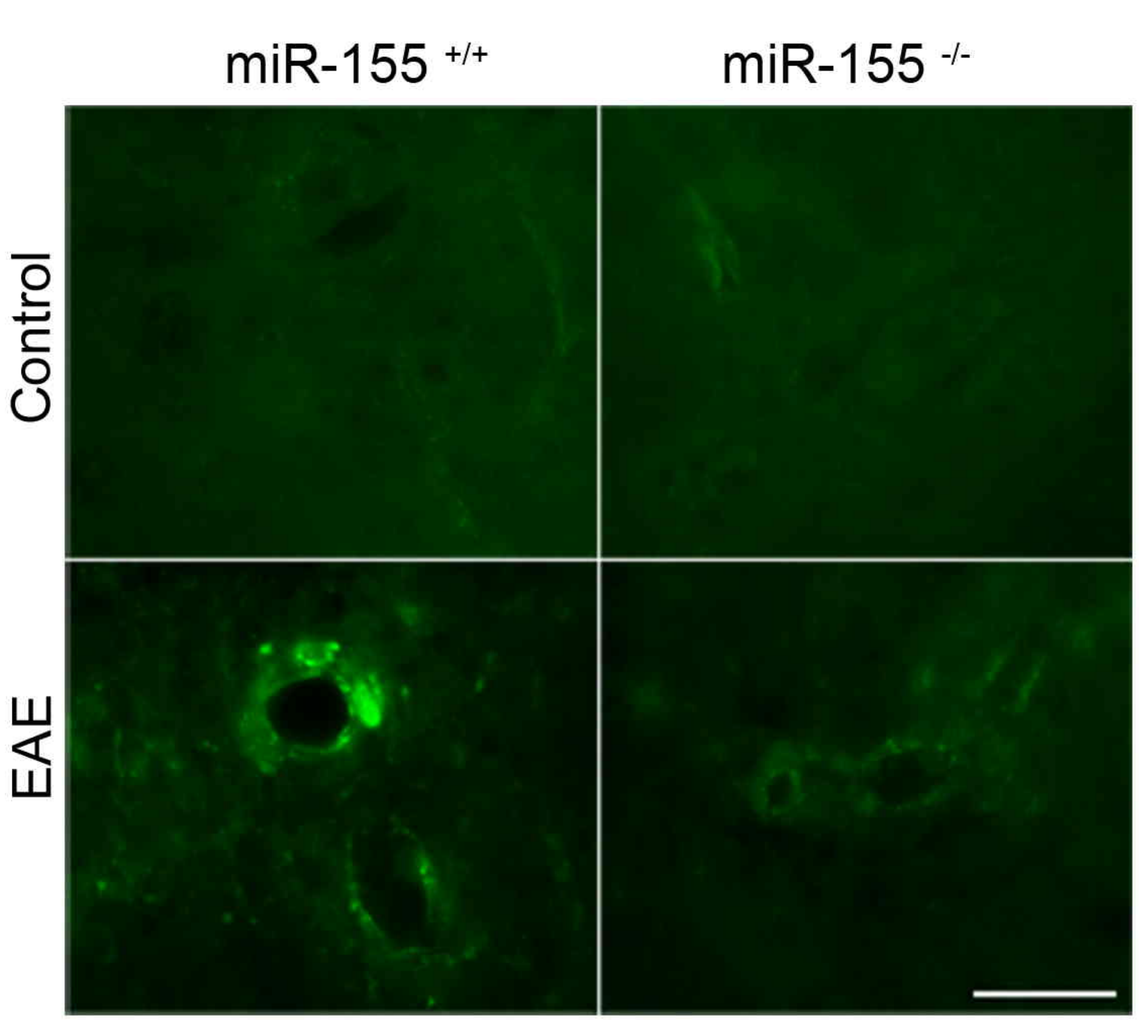

C

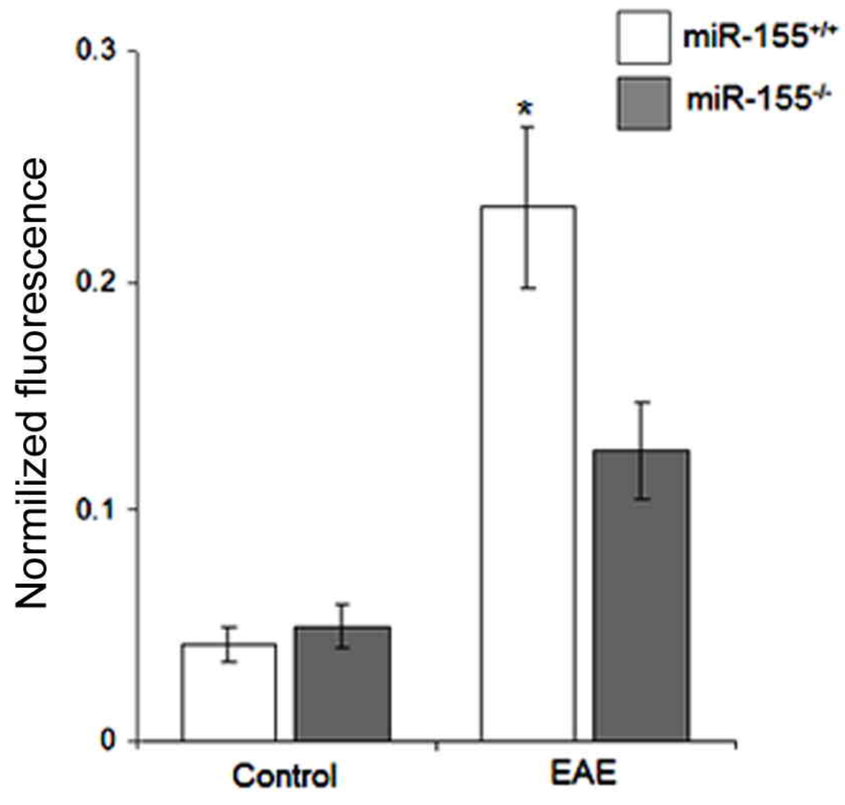

D

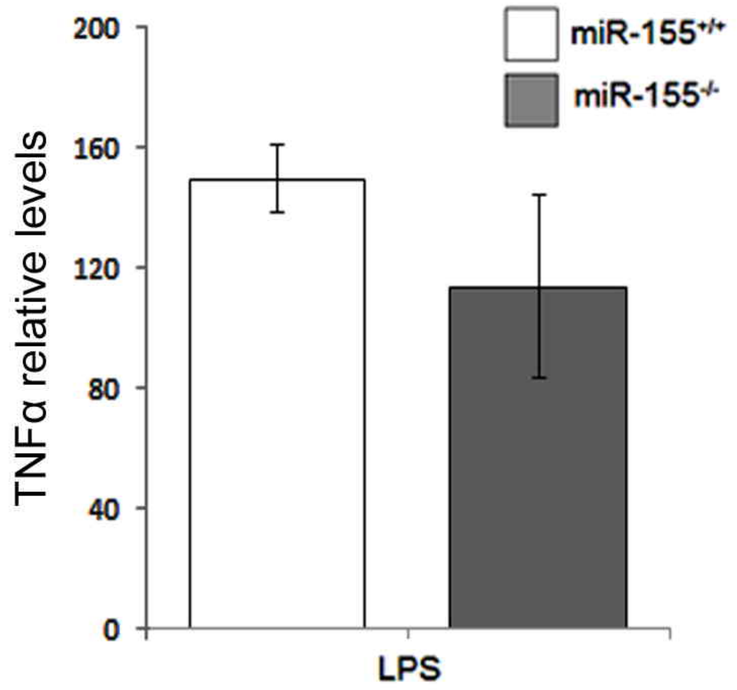

E

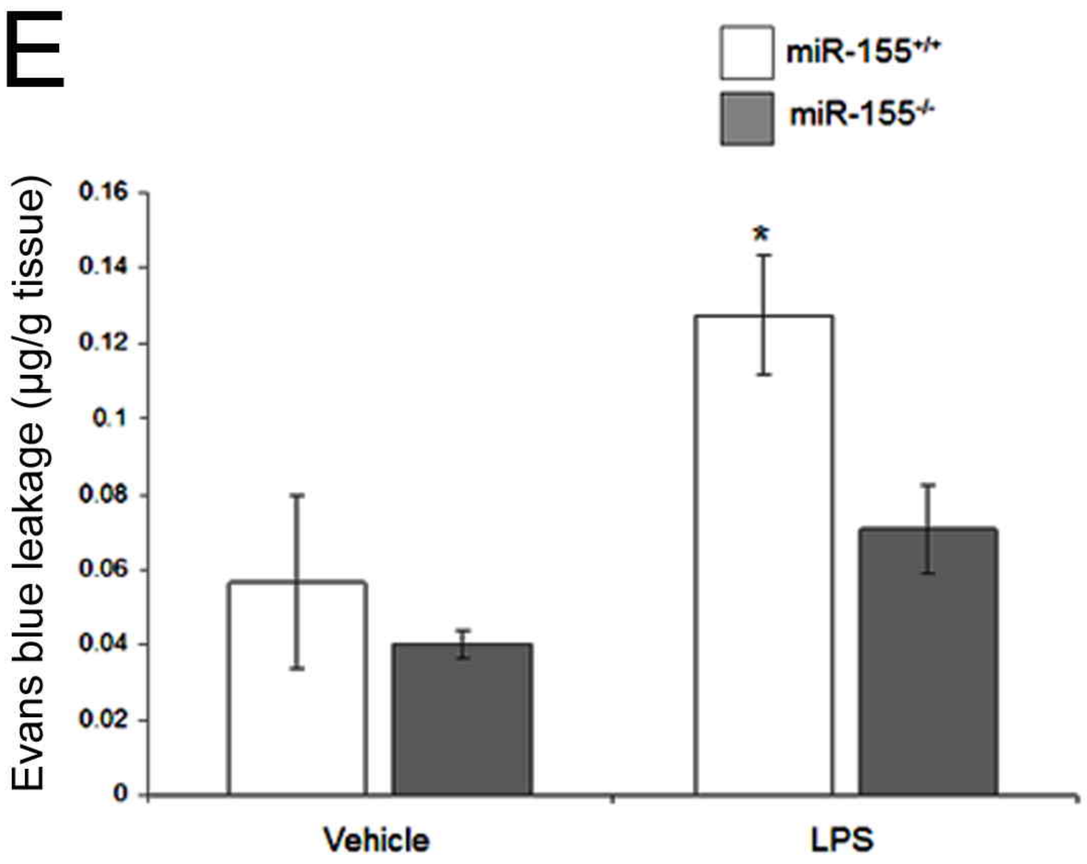

Figure 4

A

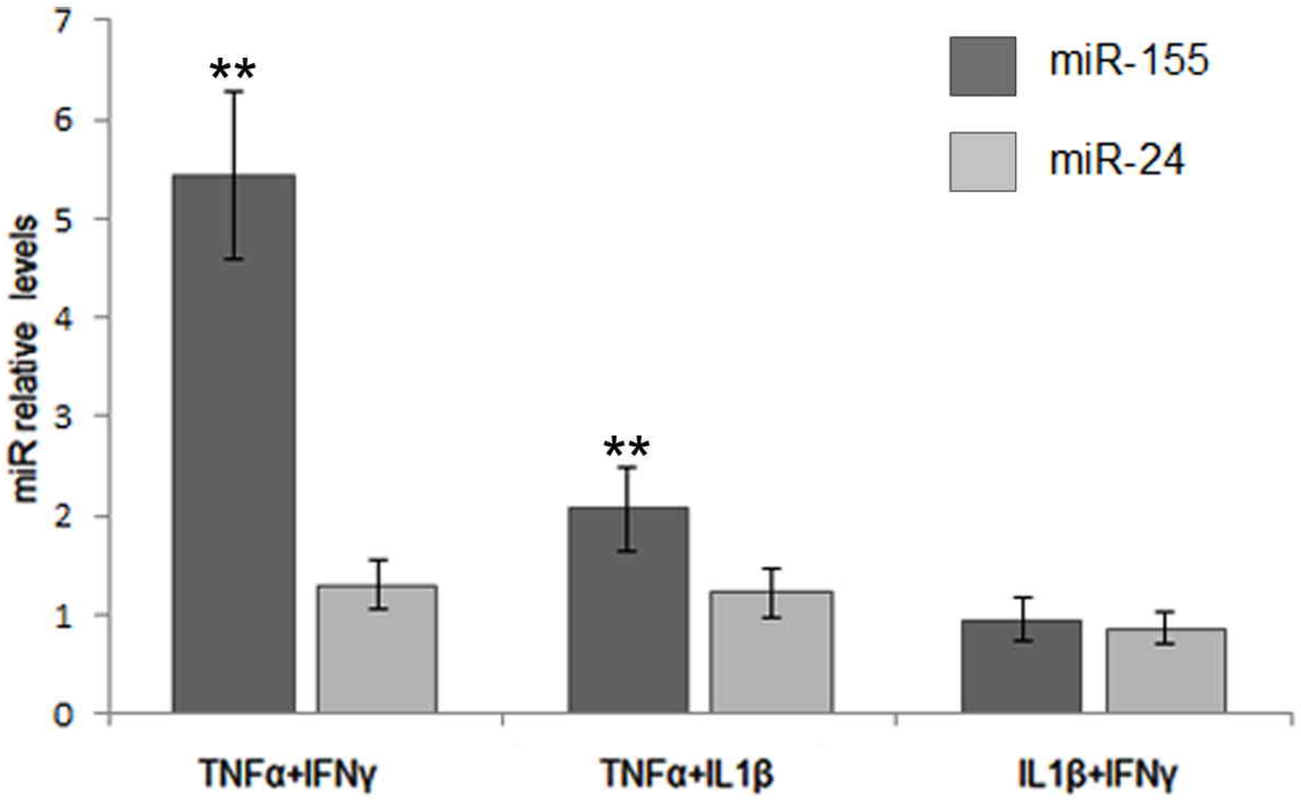

B

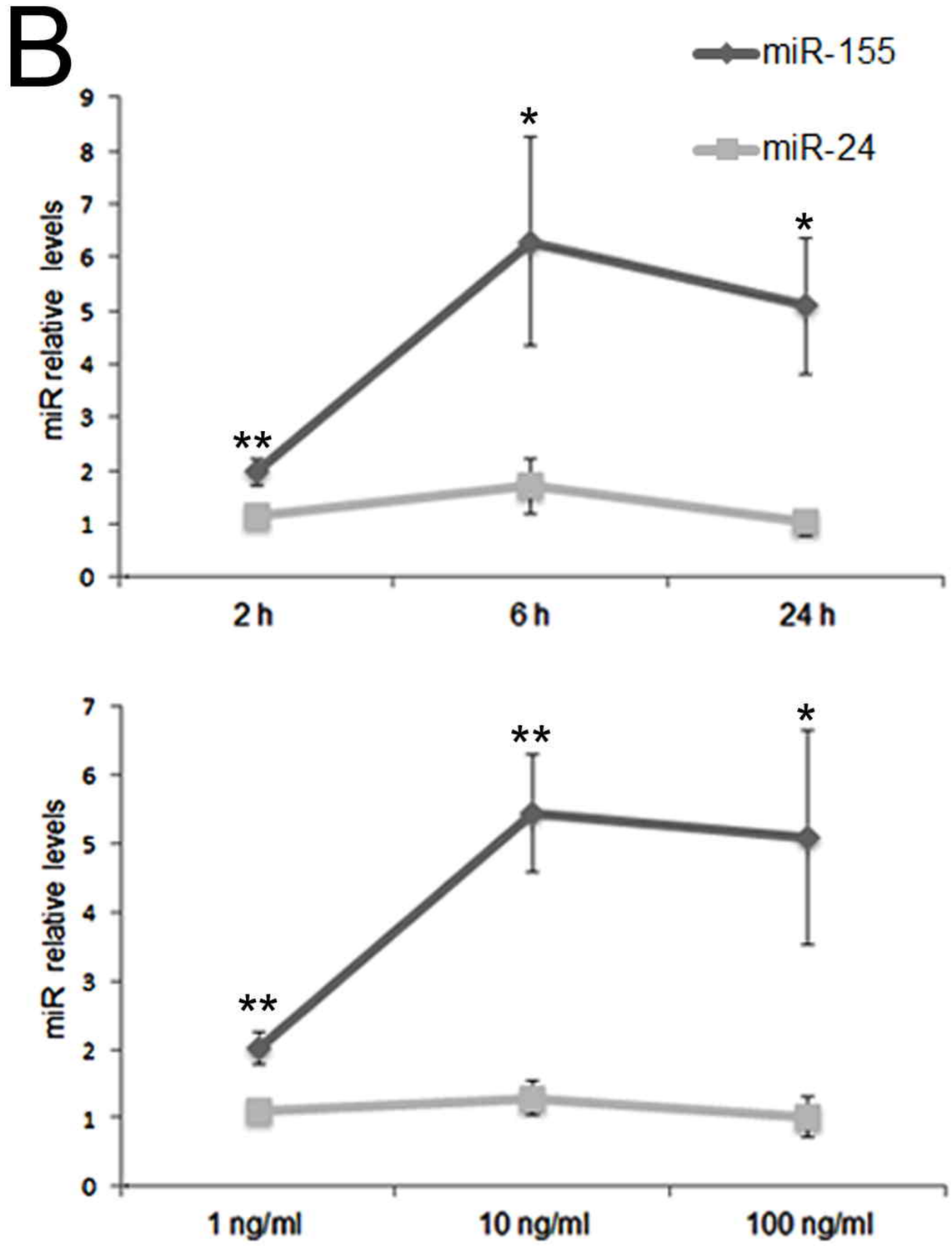

C

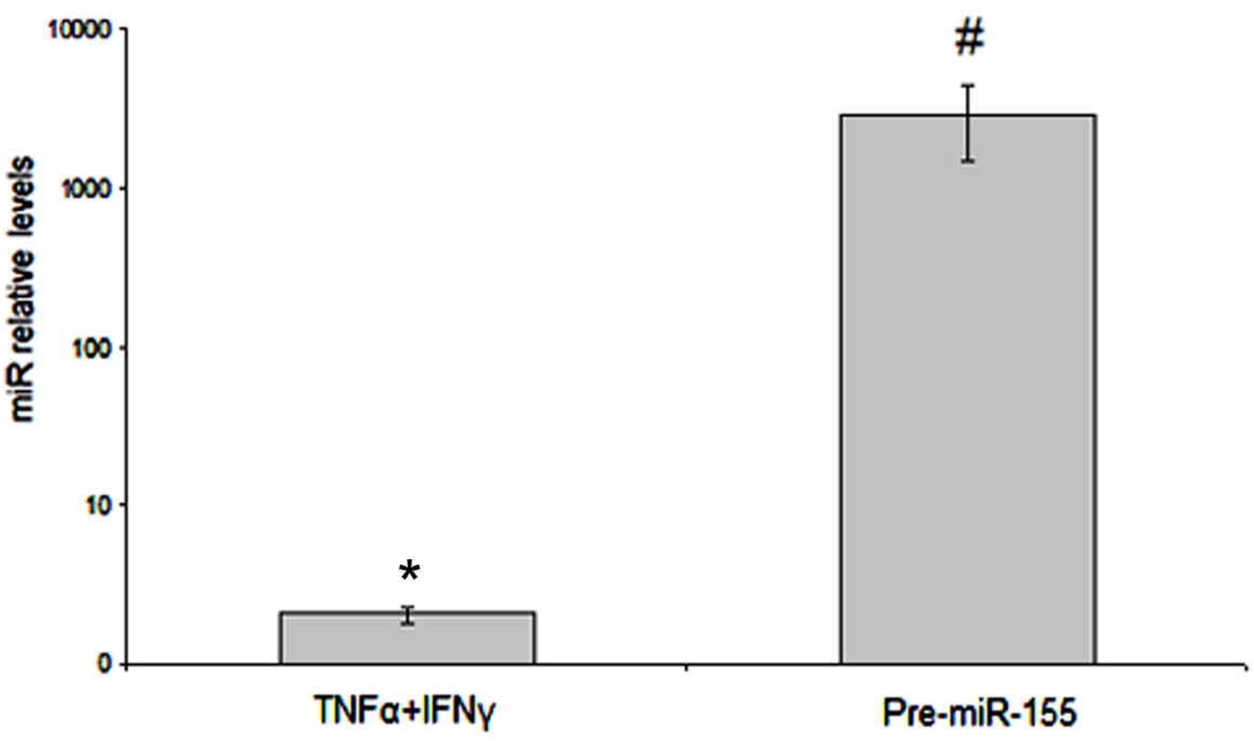

D

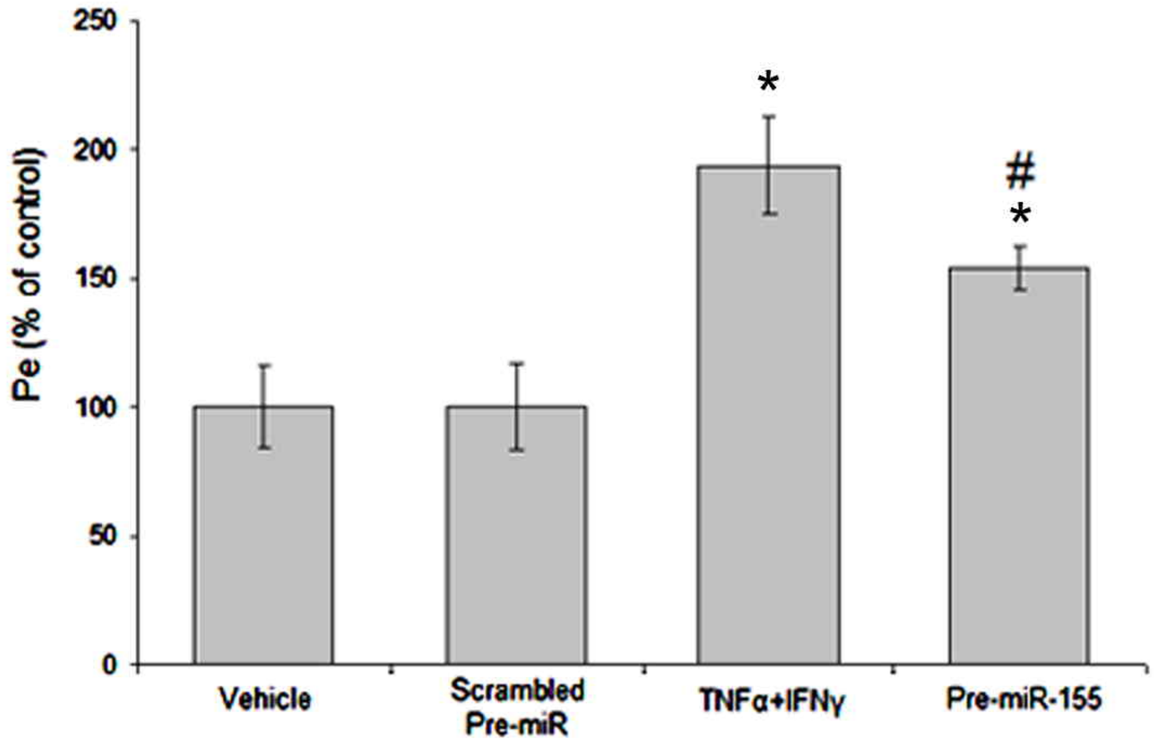

E

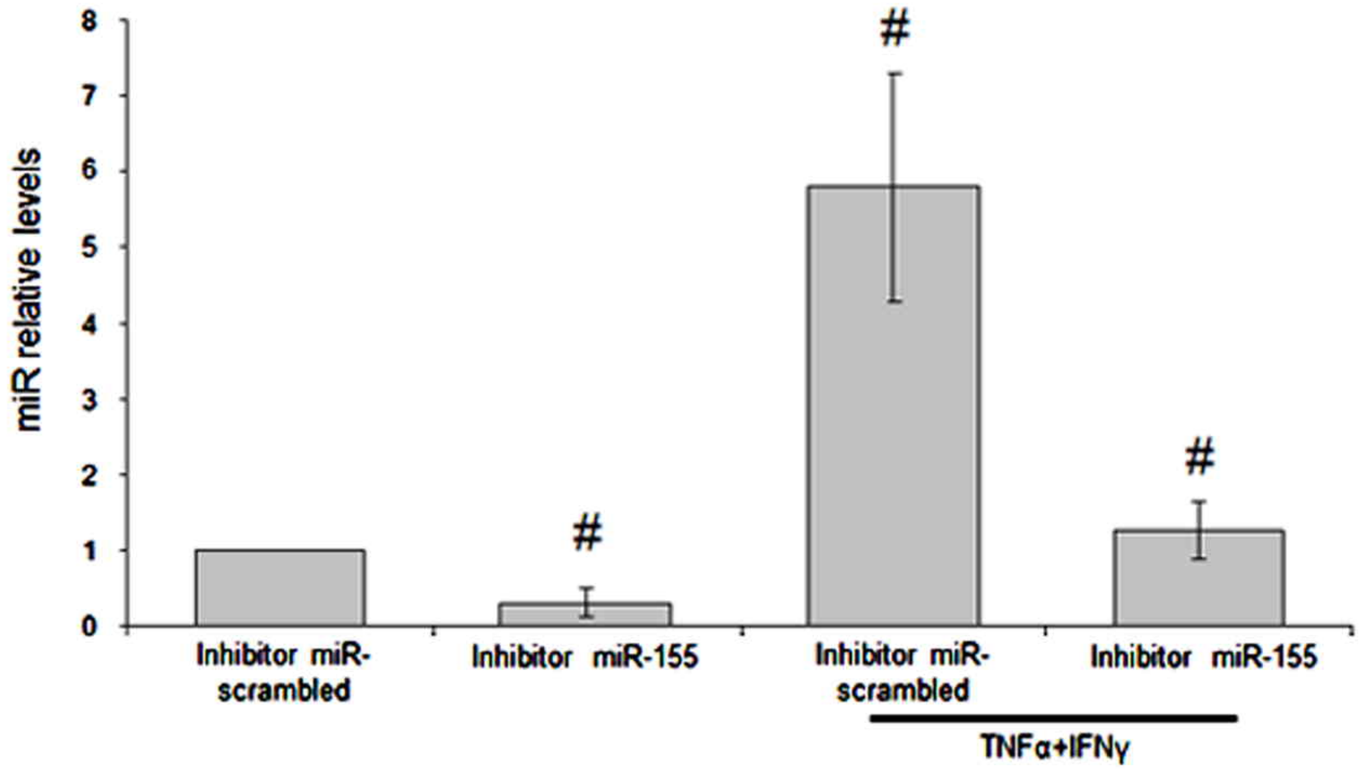

F

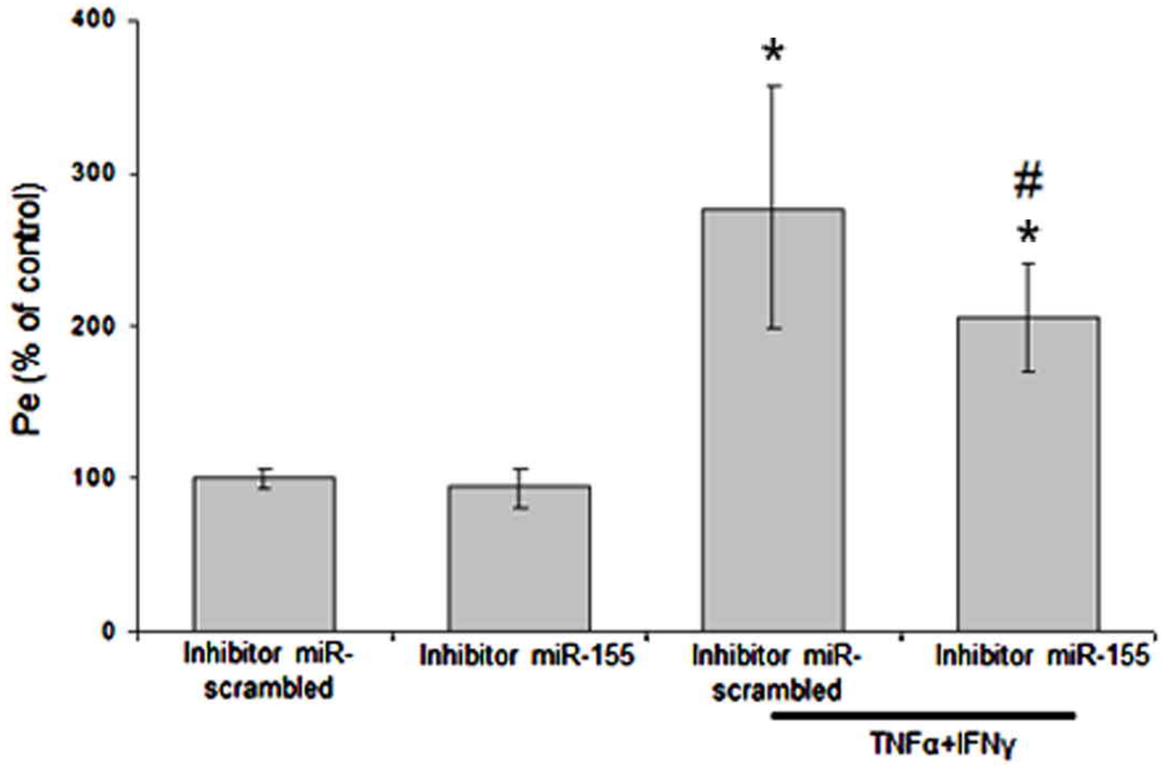

Figure 5

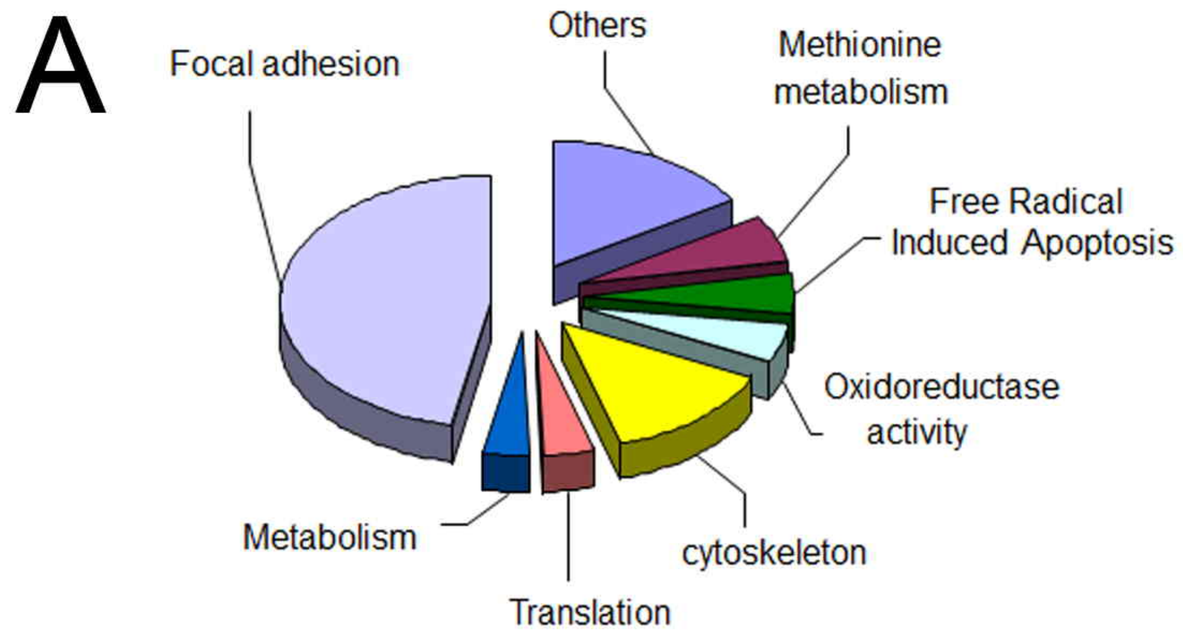
A
Focal adhesion
Others
Methionine metabolism
Free Radical Induced Apoptosis
Oxidoreductase activity
cytoskeleton
Translation
Metabolism

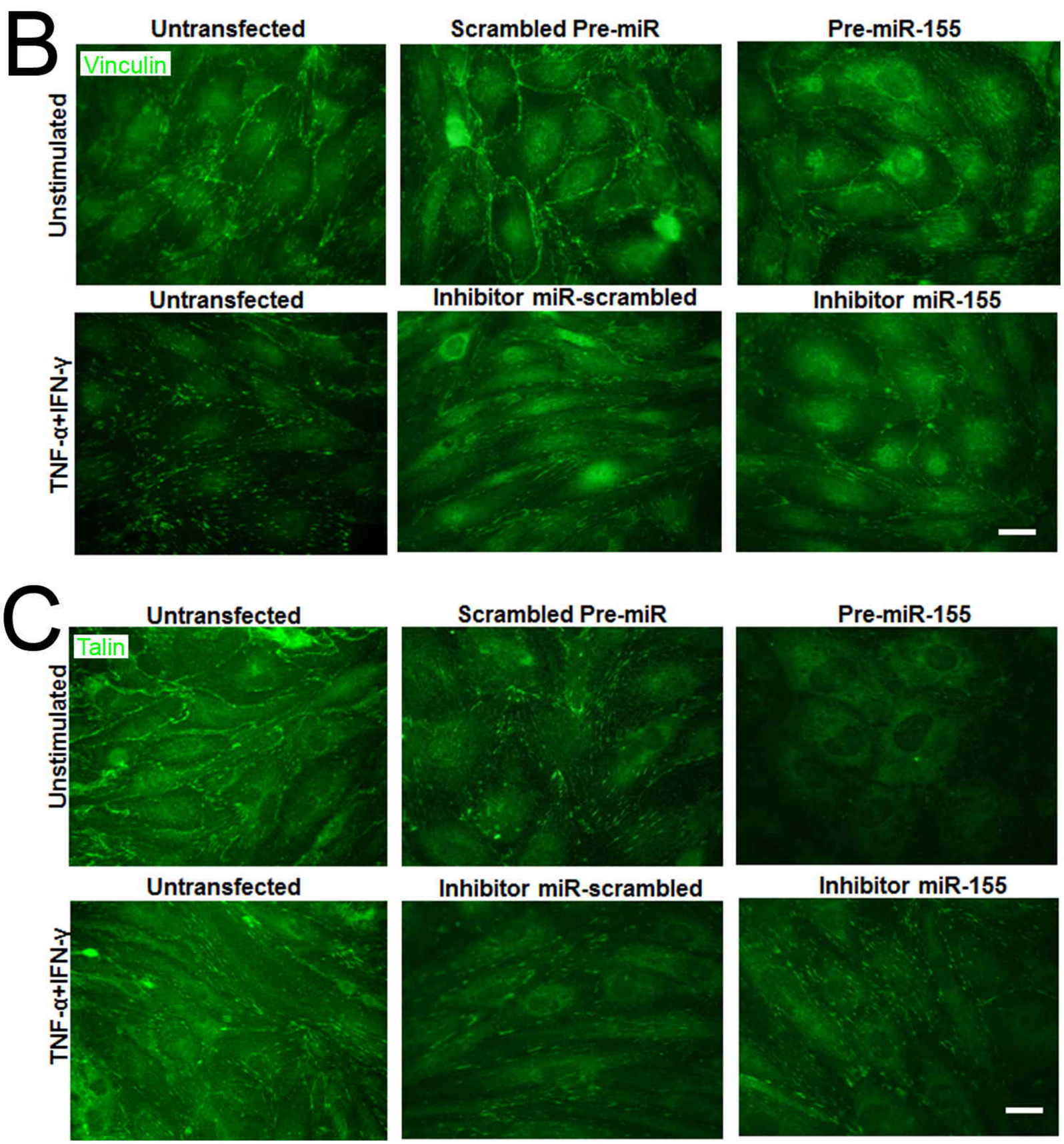
B
Untransfected
Scrambled Pre-miR
Pre-miR-155
Vinculin
Unstimulated
Untransfected
Inhibitor miR-scrambled
Inhibitor miR-155
TNF-α+IFN-γ
C
Untransfected
Scrambled Pre-miR
Pre-miR-155
Talin
Unstimulated
Untransfected
Inhibitor miR-scrambled
Inhibitor miR-155
TNF-α+IFN-γ

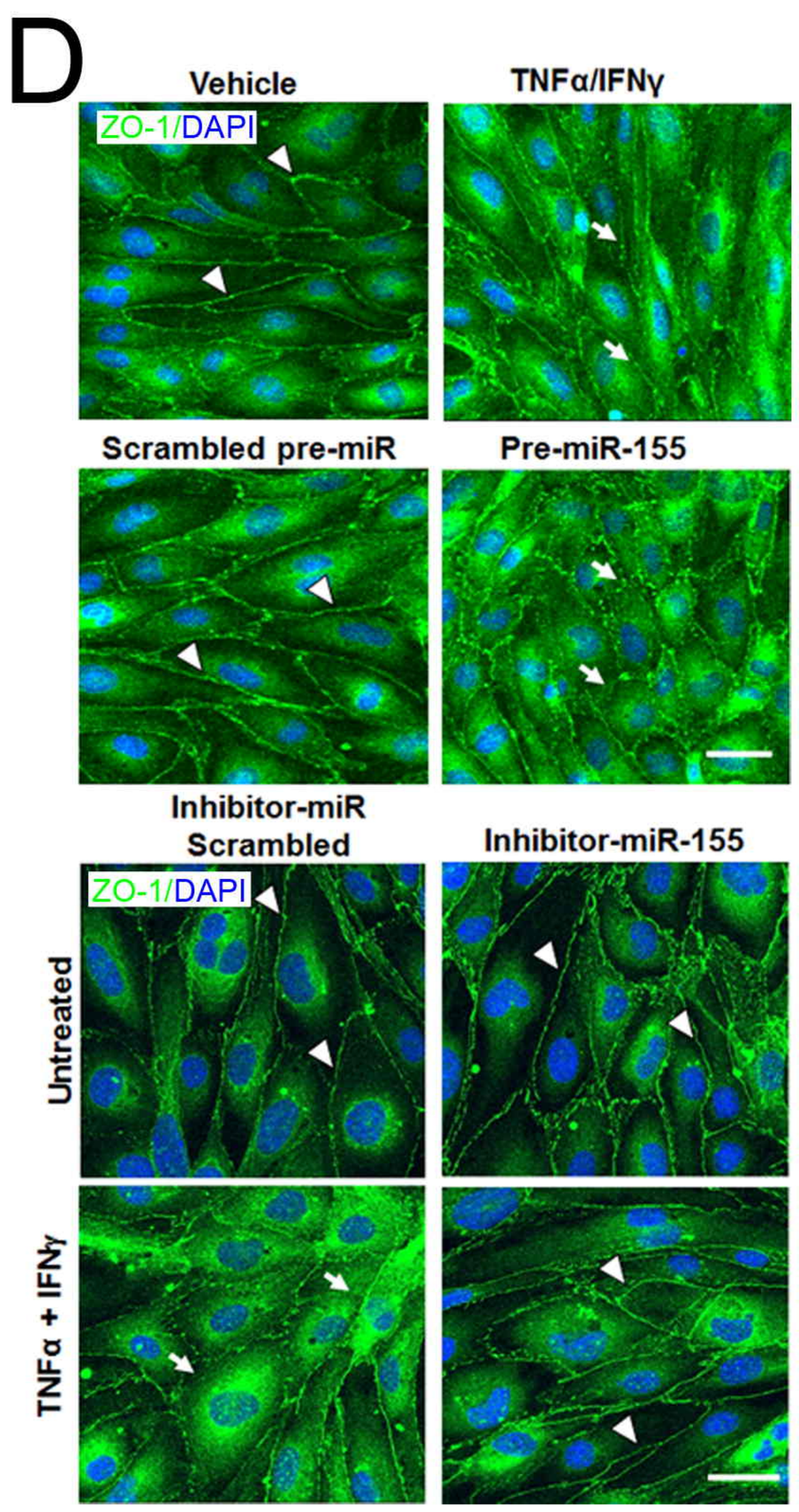
D
Vehicle
TNFα/IFNγ
ZO-1/DAPI
Scrambled pre-miR
Pre-miR-155
Inhibitor-miR Scrambled
Inhibitor-miR-155
ZO-1/DAPI
Untreated
TNFα + IFNγ

Figure 6

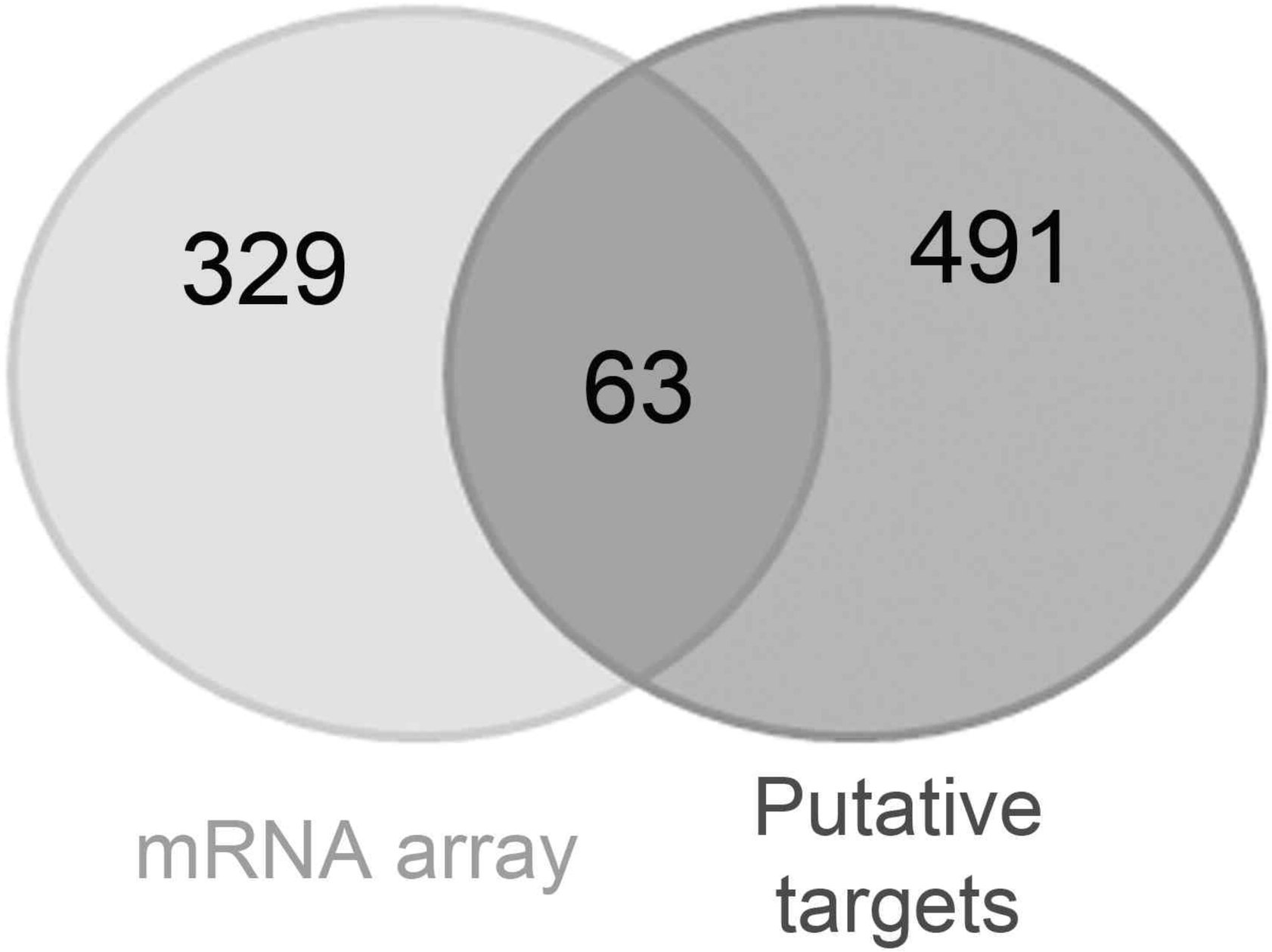

TargetScan	Guo H. (HeLa)	Selbach M. (HeLa)	Xu G. (B cells)	Downregulated in hCMEC/D3 cells	Gene symbol	Gene name	Focal adhesion (FA)	Junctional molecule (JM)
X			X	X	CLDN1	claudin-1		JM
X	X			X	ANXA2	annexin A2		JM
X	X			X	PRNP	prion protein (p27-30)		JM
X	X	X	X	X	SDCBP	syntenin-1	FA	
X	X			X	DOCK1	dedicator of cytokinesis 1	FA	
X	X			X	PALLD	palladin	FA	
X	X			X	ITGAV	integrin alpha V	FA	

Figure 7

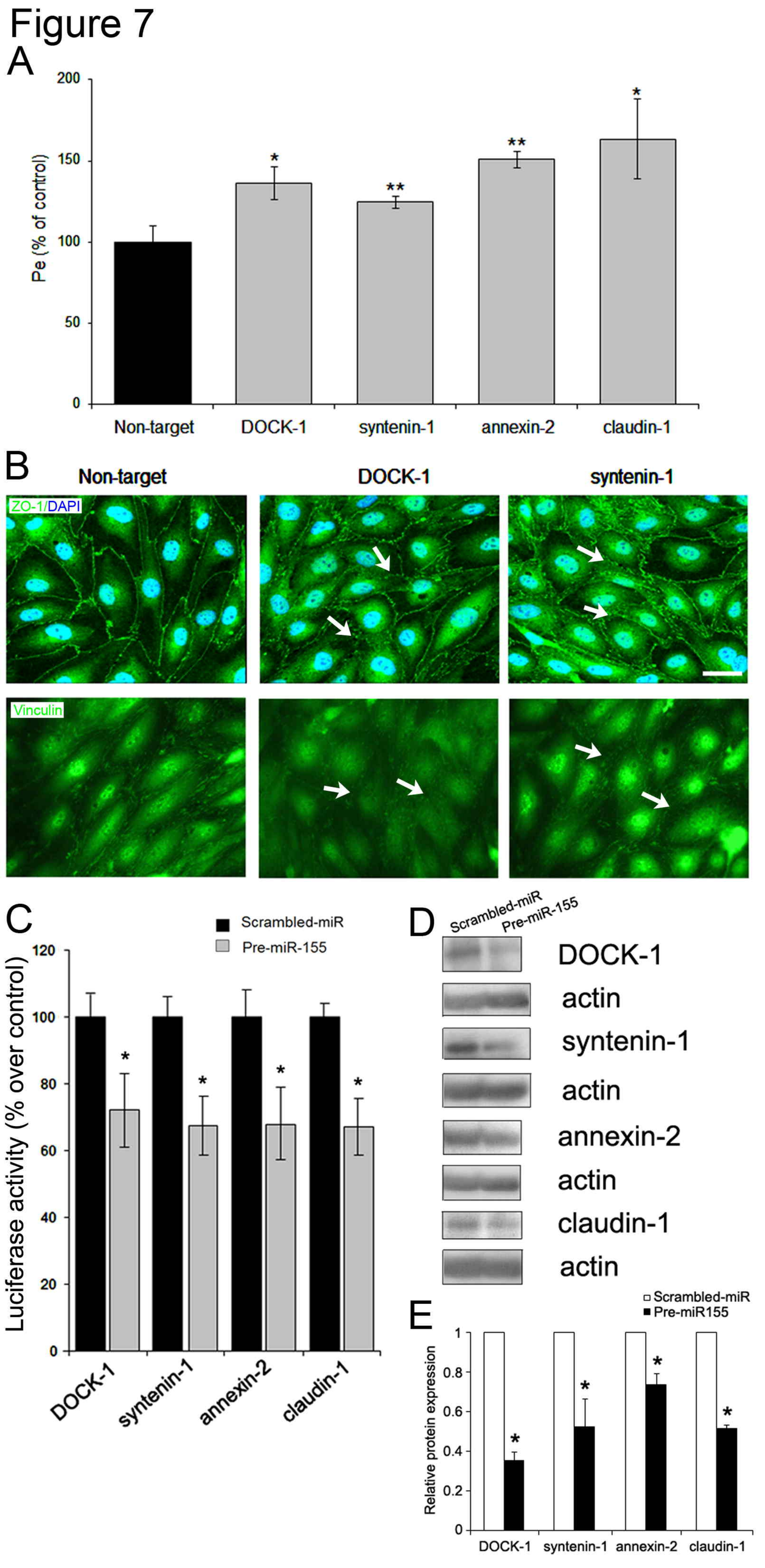
A
Pe (% of control)
200
150
100
50
0
Non-target
DOCK-1
syntenin-1
annexin-2
claudin-1
B
Non-target
DOCK-1
syntenin-1
ZO-1/DAPI
Vinculin
C
Scrambled-miR
Pre-miR-155
Luciferase activity (% over control)
120
100
80
60
40
20
0
DOCK-1
syntenin-1
annexin-2
claudin-1
D
Scrambled-miR
Pre-miR-155
DOCK-1
actin
syntenin-1
actin
annexin-2
actin
claudin-1
actin
E
Scrambled-miR
Pre-miR155
Relative protein expression
1
0.8
0.6
0.4
0.2
0
DOCK-1
syntenin-1
annexin-2
claudin-1

Supplementary information.

Supplementary Methods.

Laser capture microdissection of microvessels in human brain sections

Laser capture microdissection (LCM) was used to isolate microvessels from active lesions and normal appearing white matter of MS brains and from white matter of control brains using a rapid staining protocol. Briefly, frozen sections of 10 μm thickness were mounted on uncoated slides. Next, the tissue was fixed in cold acetone (maintained at 4 °C) for 3 min at RT. Sections were air-dried for 1 min and rapidly stained using toluidine blue solution for 1 min at RT. To eliminate the excess of toluidine blue staining, slides were rinsed in diethyl pyrocarbonatetreated deionized water and dehydrated in a graded series of ethanol [70 %, 80 %, 90 % and 100 %; (v/v)] for 10 s in each solution. Slides were finally cleared in xylene for 1 min and air-dried at RT. Approximately 200 blood vessels were isolated from each case using PixCell II laser capture microdissection system (Arcturus BioScience, Mountain View, CA, USA) and LCM-caps (Applied Biosystems, Warrington, UK).

Immunohistochemistry and *in situ* hybridization

Sections were incubated with primary antibodies rabbit anti-GLUT-1 1:100 (Merck-Millipore, Billerica, USA) in phosphate buffer saline (PBS). After washing with PBS, sections were incubated for 4 h with secondary goat anti-rat IgG conjugated to Alexa Fluor 555 (1:400, Zymed Invitrogen, Paisley, UK).

Supplemental Fig1

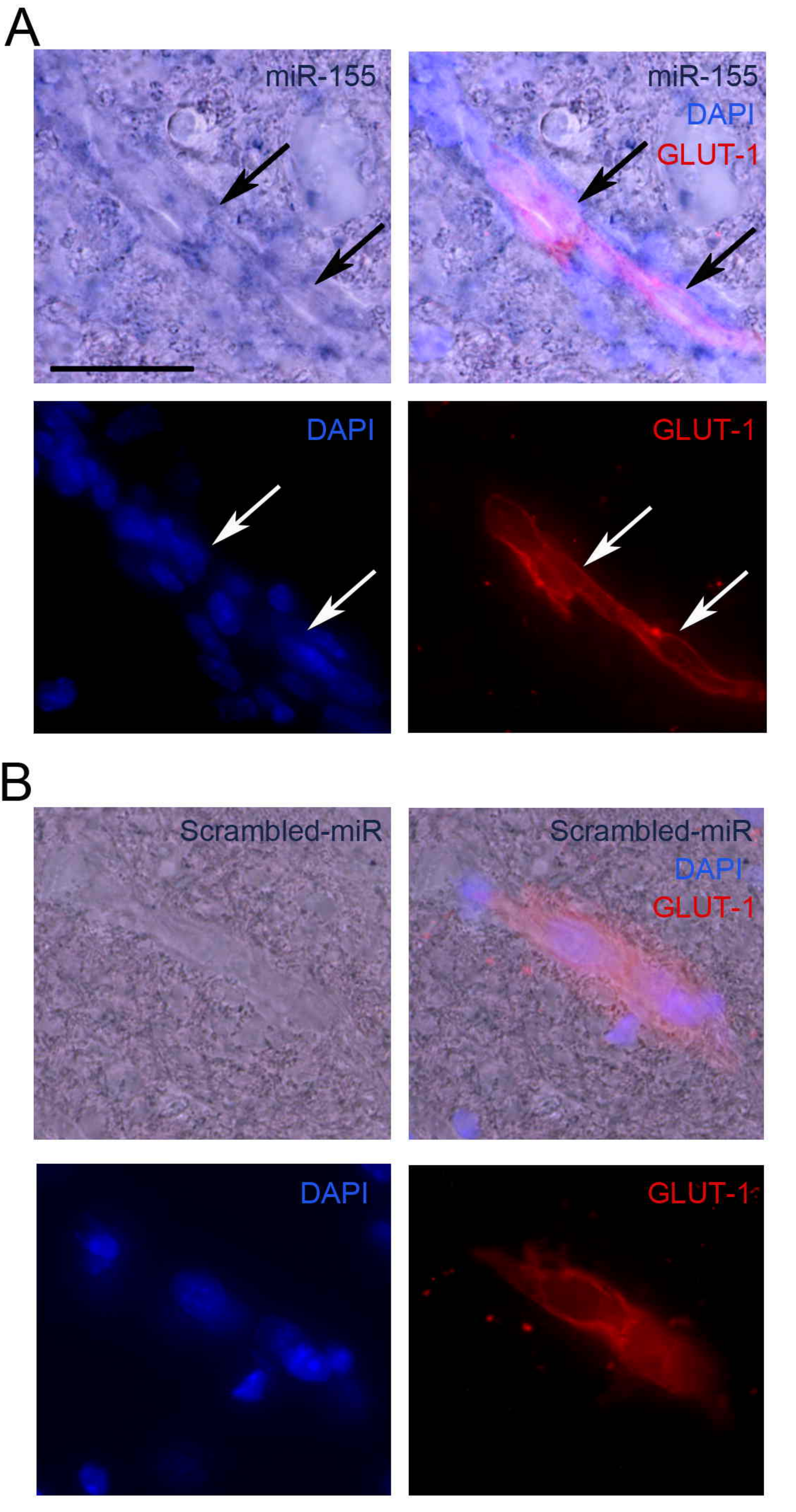

Table S1. Targetscan predicted mRNA targets for miR-155 expressed by hCMEC/D3 cells and their regulation by transfection with pre-miR-155

PROBE_ID	ACCESSION	SYMBOL	logFC	ADJ.P.VAL
ILMN_2324421	NM_182743.1	TXNRD1	-0.557288085	1.7E-05
ILMN_1703178	NM_003469.3	SCG2	-0.55585154	5.8E-03
ILMN_1724789	NM_000611.4	CD59	-0.504459026	6.3E-05
ILMN_1711899	NM_001002857.1	ANXA2	-0.460048158	4.2E-05
ILMN_1756501	NM_003032.2	ST6GAL1	-0.453081161	1.3E-03
ILMN_1717056	NM_001093771.1	TXNRD1	-0.44765833	1.1E-04
ILMN_1724686	NM_021101.3	CLDN1	-0.441355452	1.8E-04
ILMN_1783753	NM_015913.2	TXNDC12	-0.432370657	8.1E-05
ILMN_1733519	NM_005342.2	HMGB3	-0.413917585	1.2E-04
ILMN_1708016	NM_080821.2	C20orf108	-0.408461489	3.3E-04
ILMN_1769245	NM_006851.2	GLIPR1	-0.405515942	1.7E-04
ILMN_2075189	NM_017515.3	SLC35F2	-0.403517113	1.7E-04
ILMN_2360415	NM_183079.2	PRNP	-0.380844048	3.3E-04
ILMN_2094061	NM_014214.1	IMPA2	-0.377501495	2.1E-04
ILMN_1671891	NM_017933.3	PID1	-0.375489786	7.5E-04
ILMN_1769810	NM_006407.3	ARL6IP5	-0.375087151	8.5E-04
ILMN_1738383	NM_001961.3	EEF2	-0.374106404	8.5E-04
ILMN_1755937	NM_001002857.1	ANXA2	-0.372886212	3.1E-04
ILMN_2363586	NM_001007067.1	SDCBP	-0.362052767	1.9E-03
ILMN_1703060	NM_181519.2	SYT15	-0.354872236	1.4E-03
ILMN_1747160	NM_181519.2	SYT15	-0.345640411	1.3E-02
ILMN_1737988	NM_001080121.1	PRNP	-0.344880142	1.1E-03
ILMN_1667893	NM_022748.10	TNS3	-0.342774133	4.1E-03
ILMN_2169439	NM_002210.2	ITGAV	-0.340768976	1.3E-03
ILMN_1688622	NM_013438.3	UBQLN1	-0.340732475	7.1E-04
ILMN_2357062	NM_134470.2	IL1RAP	-0.338724286	7.1E-04
ILMN_1715789	NM_001380.3	DOCK1	-0.331196893	9.3E-04
ILMN_2117508	NM_138455.2	CTHRC1	-0.329325946	3.7E-03
ILMN_2316236	NM_139212.2	HOPX	-0.327274253	1.4E-03
ILMN_1746013	NM_004598.3	SPOCK1	-0.326242908	6.1E-03
ILMN_2320906	NM_006054.2	RTN3	-0.325939304	6.0E-03
ILMN_1729058	NM_004866.4	SCAMP1	-0.320643608	1.4E-03
ILMN_1708414	NM_019067.4	GNL3L	-0.320346284	3.1E-03
ILMN_1780236	NM_002676.1	PMM1	-0.317074346	6.4E-03
ILMN_2063586	NM_013943.1	CLIC4	-0.311878207	6.3E-03
ILMN_1671250	NM_013943.1	CLIC4	-0.308082947	5.2E-03
ILMN_1671404	NM_003174.3	SVIL	-0.301320871	2.7E-03
ILMN_1688753	NM_014754.1	PTDSS1	-0.300595598	4.3E-03
ILMN_2082244	NM_001037165.1	FOXK1	-0.300532441	2.5E-03
ILMN_1682738	NM_005902.3	SMAD3	-0.297799425	4.0E-03
ILMN_1707077	NM_002959.4	SORT1	-0.296641009	1.9E-03
ILMN_1804277	NM_152594.1	SPRED1	-0.296399448	2.7E-03
ILMN_1769191	NM_016592.2	GNAS	-0.296272717	1.6E-03
ILMN_1769191	NM_016592.2	GNAS	-0.296272717	1.6E-03
ILMN_1736704	NM_001037954.2	DIXDC1	-0.294865454	4.4E-03
ILMN_1743714	NM_014550.3	CARD10	-0.29450325	5.6E-03
ILMN_2393763	NM_001024960.1	ARPC4	-0.291570641	4.4E-03
ILMN_1766169	NM_005504.4	BCAT1	-0.289374644	4.8E-03

ILMN_1651347	NM_014755.1	SERTAD2	-0.288753138	2.7E-03
ILMN_2176768	NM_012247.3	SEPHS1	-0.286872143	8.6E-03
ILMN_1788701	NM_033222.2	PSIP1	-0.284419562	5.5E-03
ILMN_1751097	NM_194071.2	CREB3L2	-0.280735738	2.9E-03
ILMN_1679796	NM_014765.1	TOMM20	-0.280336735	3.5E-03
ILMN_1769517	NM_001081640.1	PRKDC	-0.278718443	5.9E-03
ILMN_1720965	NM_001007466.1	TULP4	-0.27835712	7.8E-03
ILMN_2272876	NM_031912.3	SYT15	-0.276205853	8.7E-03
ILMN_1737184	NM_031942.4	CDCA7	-0.272470028	4.0E-03
ILMN_1698323	NM_001031706.1	PLEKHB2	-0.267386789	7.1E-03
ILMN_2374865	NM_001040619.1	ATF3	-0.267156301	7.3E-03
ILMN_1779886	NM_020773.1	TBC1D14	-0.262649064	7.7E-03
ILMN_2253648	NM_006904.6	PRKDC	-0.260542479	1.9E-02
ILMN_1727194	NM_001219.2	CALU	-0.25793313	8.2E-03
ILMN_1698732	NM_016081.3	PALLD	-0.244394702	7.7E-03
ILMN_1719972	NM_017514.2	PLXNA3	-0.23564954	8.2E-03
ILMN_2157951	NM_005819.4	STX6	-0.235620546	8.2E-03
ILMN_2188264	NM_001554.3	CYR61	-0.235507217	9.9E-03
ILMN_1800634	NM_005009.2	NME4	-0.230180068	9.9E-03
ILMN_2375830	NM_001037954.2	DIXDC1	-0.22456104	1.8E-02
ILMN_2337740	NM_020245.3	TULP4	-0.212661064	3.2E-02
ILMN_2363065	NM_201430.1	RTN3	-0.2083027	2.7E-02
ILMN_2297710	NM_017958.1	PLEKHB2	-0.194937569	3.2E-02
ILMN_2313821	NM_145813.1	AIFM1	0.259641014	4.9E-03